DIFFERENT PARTICLE SIZE INFORMATION OBTAINED FROM STATIC AND DYNAMIC LASER LIGHT SCATTERING

by

Yong Sun

B.Sc., Zhengzhou University, China, 1990

M.Sc., University of Science and Technology of China, China, 1996

A THESIS SUBMITTED IN PARTIAL FULFILLMENT
OF THE REQUIREMENTS FOR THE DEGREE OF
MASTER OF SCIENCE
in the Department
of
Physics

SIMON FRASER UNIVERSITY
August 2004

APPROVAL

Name: Yong Sun

Degree: Master of Science

Title of thesis: Different Particle Size Information Obtained from Static and Dynamic Laser Light Scattering

Examining Committee: Dr. Howard Trottier, Professor
Chair

Dr. Barbara Frisken, Professor
Senior Supervisor, Department of Physics

Dr. John Bechhoefer, Professor
Department of Physics

Dr. David Boal, Professor
Department of Physics

Dr. Arthur Bailey
Scitech Instruments

Dr. Michael Hayden, Associate Professor
Internal Examiner, Department of Physics

Date Approved: August 16, 2004

SIMON FRASER UNIVERSITY

Partial Copyright Licence

Abstract

Static light scattering (SLS) and dynamic light scattering (DLS) techniques are used to measure characteristics of particles in dispersion. SLS measures the dependence of the average scattered intensity I_s on the scattering angle and is sensitive to spatial variations in the dielectric constant ε. DLS measures the time dependence of the scattered light. One fundamental application of light scattering techniques is the accurate measurement of the size distribution of particles in dispersion.

Detailed experimental investigation of SLS and DLS has been attempted in this work, with experimental work based on dilute water dispersions of two different spherical particles, polystyrene latexes and poly(N-isopropylacrylamide) ($PNIPAM$) microgels. Size information is obtained from SLS measurements in the form of a particle size distribution $G(R_s)$ where R_s is the static radius. Size information is obtained from DLS measurements in the form of a decay rate distribution $G(\Gamma)$ which depends on the decay rate Γ.

Although both SLS and DLS can be used to obtain size information from the scattered light, the information obtained using SLS and DLS is different. For the three polystyrene latex sphere samples studied in this thesis, the mean static radii obtained are consistent with that of the mean radii provided by the supplier. For all three samples, the apparent hydrodynamic radius is larger than the mean static radius by about 12%. For PNIPAM microgel spheres, the apparent hydrodynamic radius is also larger than the mean static radius. The size of the PNIPAM microgel particles is extremely temperature sensitive; the radius decreases by a factor of three as the temperature is raised from 15°C to 50°C. Both the hydrodynamic and static radii show this behavior. The effect of the chemical crosslinker (N, N'-methylenebisacrylamide) content on the temperature sensitivity of the PNIPAM microgels and the temperature dependence of the ratio of the apparent hydrodynamic radius to the mean static radius are also discussed.

Acknowledgments

I would like to thank Dr. Barbara Frisken, for providing me with the opportunity to study a challenging project in which I am very interested and for her guidance through this thesis. I would like to thank my committee members, Dr. David Boal, Dr. John Bechhoefer and Dr. Arthur Bailey, for their input and advice.

I really appreciate Dr. Jun Gao for making the PNIPAM microgel samples and helping me to understand the chemical structures of the samples. I would like to thank those who shared the lab with me: Laurent Rubatat, David Lee, Philip Patty and Kevin Stevenson and I also would like to thank other people with whom I take pleasure in collaborating at Simon Fraser University.

Contents

List of Tables

List of Figures

Chapter 1

Introduction

A great deal of information about particles in dispersion can be obtained using light scattering techniques. Two important techniques are static light scattering (SLS) and dynamic light scattering (DLS). SLS measures the dependence of the average scattered intensity on the scattering angle. Structural information about the particles, including the size, shape and molar mass, can be obtained using SLS. DLS measures the time autocorrelation of the scattered light intensity $g^{(2)}(\tau)$ as a function of the delay time τ. The results obtained from DLS provide dynamic information about the particles in dispersion including translational, rotational and internal motion. One fundamental application of light-scattering techniques is the accurate measurement of the size distribution of particles in dispersion.

Different methods have been used to obtain structural information from SLS measurements depending on the values of $q\left\langle R_g^2\right\rangle^{1/2}$, where q is the scattering vector and $\left\langle R_g^2\right\rangle^{1/2}$ is the radius of gyration of particles. For small $q\left\langle R_g^2\right\rangle^{1/2}$, the SLS measurements are simplified to the Zimm plot [1], Berry plot or Guinier plot [2] etc., where the experimental data are plotted in different forms to obtain a linear plot region, so the root mean-square radius of gyration $\left\langle R_g^2\right\rangle^{1/2}$ and the molar mass of particles can be easily obtained. Since all information is obtained under the condition that the values of $q\left\langle R_g^2\right\rangle^{1/2}$ are small, most information contained in SLS is neglected. If the information at large values of $q\left\langle R_g^2\right\rangle^{1/2}$ is considered by fitting a form factor to the SLS data, more detailed information can be obtained. Since the same constraints $\left(q\left\langle R_g^2\right\rangle^{1/2} \ll 1\right)$ that apply to the Zimm plot, Berry plot or Guinier plot do not apply when fitting a form factor to the data, size distributions for much larger particles can be obtained from SLS measurements.

How the particle size distribution can be obtained directly from SLS data has been

studied by various authors. For example, Schnablegger and Glatter [3] assumed that the size distribution can be described as a series of cubic B-splines and used simulated data and measured data to demonstrate their computation procedure. Strawbridge and Hallett [4] studied the scattered intensity of coated spheres. They used a discrete method to obtain particle size distributions minimizing $[I(q) - \sum_{n=1}^{m} a_n I(q, r_n)]^2$, where $I(q)$ is the scattered intensity of measurements, $I(q, r_n)$ is the scattered intensity of a particle with a chosen geometrical or linear trial radius between r_{min} and r_{max} and a_n is constrained to be positive and represents the amplitudes of a histogram.

In this thesis, a equation for homogenous spherical particles is used to obtain the size distribution and the average molar mass for large particles from SLS. In this equation, a Gaussian distribution is chosen to represent the particle size distribution and size information is obtained by fitting the equation to the data in terms of the static radius R_s and the width of the distribution σ.

Traditionally, two standard methods have been used to obtain size information about dispersed particles from DLS data: moment analysis [[5] – [9]] and the inverse Laplace transform algorithm, which involves solving an ill-conditioned problem [10]. Both provide information about the hydrodynamic radius R_h. Although R_h can be measured accurately at a given scattering angle using moment analysis, R_h shows a strong dependence on the scattering vector q. This occurs because the DLS data is intensity-weighted and in most cases larger particles scatter more light. Moment analysis does not take this intensity-weighted difference into account. Moment analysis is also relatively insensitive to a small degree of polydispersity. In order to detect small degrees of polydispersity, for dilute polydisperse homogeneous spherical particles, Pusey and van Megen [12] proposed a method to accurately detect small polydispersities when the Rayleigh-Gans-Debye (RGD) approximation is valid by measuring the dependence of the effective diffusion coefficient $D \propto \frac{1}{R_h}$ on the scattering angle. Both theoretical and experimental results show that the angular dependence of the effective diffusion coefficient is a sensitive function of the particle's size and distribution.

In order to obtain more accurate information about particles, people have explored relationships between the physical quantities obtained using SLS and DLS techniques. Some researchers use the dimensionless shape parameter $\rho = \langle R_g^2 \rangle^{1/2} / R_h$ to determine the particle shape [[2], [13] – [15]]. Others [11] have investigated the particle size distribution of homogenous spherical particles by comparing the q-dependence of the apparent hydrodynamic radius $R_h(q)$ and the average scattered intensity for three distributions: Gaussian,

Log normal and Weibull. Their results show that sometimes the q-dependence of R_h can be used to distinguish between distributions while the q-dependence of I is relatively insensitive to the distribution used.

There is a potential problem with these analyses for polydisperse samples. Different sizes contribute with different weights to the scattered intensity. For example, at small scattering angles, most of the scattered intensity comes from the larger size particles. For the Zimm plot analysis, which is applied at small scattering angles, the values of $\langle R_g^2 \rangle^{1/2}$ will be dominated by these larger particles. The values of R_h are also influenced by the scattered intensity and can depend on scattering angle. For small particles, where R_h is basically independent of q and R_g is well-defined, ρ has been used to judge the shape of particles for a long time. The use of ρ as a test for the shape of small particles will be discussed again in this work. The static radius R_s, obtained directly from SLS, provides a method that examines the validity of the dimensionless shape parameter ρ, because, from the definition $\langle R_g^2 \rangle^{1/2}$, it is a function of static radius R_s and distribution $G(R_s)$.

In our experiments, two different kind samples were studied: polystyrene and PNIPAM microgel particles. The size distribution was investigated using SLS and DLS. Commercial polystyrene spheres are used as standard particles for comparing the results obtained using Transmission Electron Microscopy (TEM), SLS and DLS. Our results show that the values of mean static radius and the mean radius measured using TEM are consistent while the value of R_h is larger than that of mean static radius under the same conditions.

PNIPAM microgel particles belong to a class of synthetic aqueous microgels that displays extreme temperature sensitivity [16], most of which are based on poly(N-isopropylacrylamide) ($PNIPAM$) or related copolymers. PolyNIPAM is a polymer which has a critical solution temperature about 32°C in water. As temperature increases above the critical temperature, the interaction of PNIPAM microgels with water molecules changes from being hydrophilic to hydrophobic. Their volumes collapse and the PNIPAM microgels undergo a volume phase transition. Many authors [[17], [18]] have measured the equilibrium swelling ratios of polyNIPAM hydrogels with different levels of crosslinking using DLS techniques. The ratios are then used to identify the phase transition. Some authors [[19] – [21]] have also measured the dimensionless shape parameter ρ as a function of the temperature. Their results show that R_h/R_g has a peak in the vicinity of the phase transition temperature.

Both SLS and DLS measurements were made on PNIPAM samples. The SLS data thus were analyzed and the size distribution of the particles was obtained. Our results show

that the size distribution of PNIPAM microgels, even with a small degree of polydispersity that cannot be measured using moment analysis , can be measured accurately. The mean static radii of PNIPAM microgels at different temperatures have been used to indicate the volume phase transition. The effects of changing the amount of crosslinker was also investigated. The apparent hydrodynamic radii were obtained from DLS measurements using moment analysis. The same phase transition was observed using the hydrodynamic radii. Comparison of the hydrodynamic radius and the static radius shows that the value of R_h is larger than that of $\langle R_s \rangle$ under the same conditions for PNIPAM samples. For the particular volume phase transition of PNIPAM microgel samples, the negative thermal expansion coefficient also was discussed. With experimental data analysis, better understanding of the size information contained in DLS and SLS spectroscopies was obtained.

Chapter 2

Light Scattering Theories

Light scattering is caused by inhomogeneities of the dielectric constant of the scattering medium. In particle dispersions, the intensity of the scattered light depends on the sizes and shapes of the particles as well as interparticle interactions. In this Chapter, the scattering geometry being used and static and dynamic light scattering theories will be discussed.

2.1 Scattering Geometry

A nonmagnetic, nonconducting, nonabsorbing medium is considered. If this medium is not optically uniform, i.e. if there are spatial and/or temporal fluctuations of the dielectric constant, light is scattered away from the direction of incidence. The local dielectric tensor $\epsilon(\vec{r},t)$ of the medium can be expressed in terms of an average dielectric constant and a fluctuating component $\delta\varepsilon(\vec{r},t)$,

$$\varepsilon(\vec{r},t) = \varepsilon_0 I + \delta\varepsilon(\vec{r},t), \tag{2.1}$$

where I is the second rank unit tensor. The incident electric field $\vec{E}(\vec{r},t)$ can be written

$$\vec{E}(\vec{r},t) = \hat{n}_i E_0 \exp i\left(\vec{k}_i \cdot \vec{r} - \omega_i t\right), \tag{2.2}$$

where $\hat{n}_i$, E_0, $\vec{k}_i$ and ω_i are the unit vector along the direction of the incident electric field, the field amplitude, the wave vector and the angular frequency respectively. A sketch of the incident and scattered light is shown in Fig. 2.1.

If the probability of the incident photons being scattered more than once is low and the collision is elastic, the scattered electric field $\vec{E}_s(R,t)$ with polarization $\hat{n}_f$, wave vector $\vec{k}_f$,

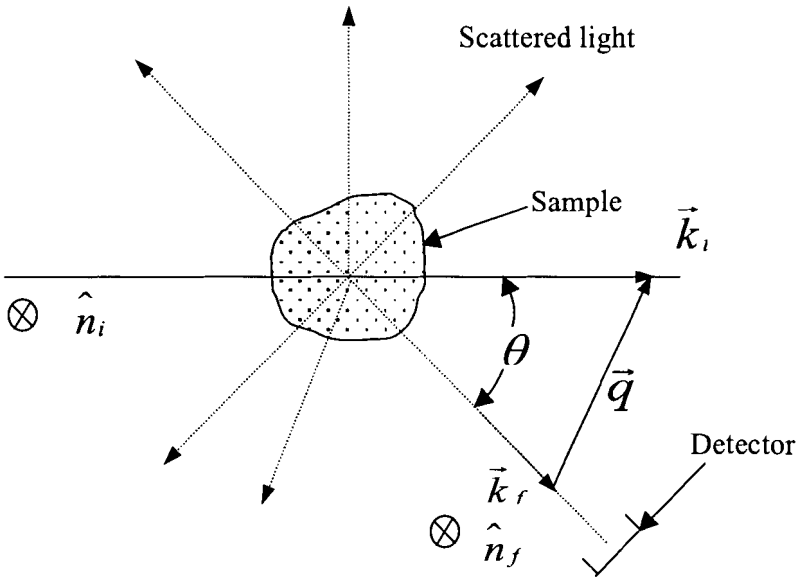

Figure 2.1: Light of polarization $\hat{n}_i$ and wave vector $\vec{k}_i$ is incident on the sample. Light is scattered in all directions as shown by the dotted arrows. The detector measures the scattered light of wave vector $\vec{k}_f$ and polarization $\hat{n}_f$. θ is the scattering angle and the scattering wave vector $\vec{q}$ is equal to $\vec{k}_i - \vec{k}_f$. $\hat{n}_i$ and $\hat{n}_f$ are perpendicular to the plane.

and frequency ω_f at a large distance R from the scattering volume can be written as [22]

$$E_s\left(\vec{R},t\right) = \frac{E_0}{4\pi\varepsilon_0 R}\exp\left(ik_f R\right)\int_v d^3r \exp\left[i\left(\vec{q}\cdot\vec{r}-\omega_i t\right)\right] \left[\hat{n}_f\cdot\left[\vec{k}_f\times\left(\vec{k}_f\times\left(\delta\varepsilon\left(\vec{r},t\right)\cdot\hat{n}_i\right)\right)\right]\right], \tag{2.3}$$

where the subscript v indicates that the integral is over the scattering volume; the scattering volume is the intersection of the incident beam with the beam that reaches the detector. The scattering wave vector $\vec{q}$ is shown in Fig. 2.1; $\vec{q}$ is defined as the difference between the directions of propagation of the incident and scattered light

$$\vec{q} = \vec{k}_i - \vec{k}_f. \tag{2.4}$$

The angle between $\vec{k}_i$ and $\vec{k}_f$, θ, is called the scattering angle. If the wave lengths in vacuo

of the incident and scattered light are λ_i and λ_f, the magnitudes of $\vec{k}_i$ and $\vec{k}_f$ are $\frac{2\pi n_s}{\lambda_i}$ and $\frac{2\pi n_s}{\lambda_f}$, respectively, where n_s is the refractive index of the scattering medium. In general, the frequency of the incident light changes little in the scattering process and the scattering process approximates an elastic collision so that

$$|\vec{k}_i| = |\vec{k}_f| = k. \tag{2.5}$$

From Eqs. 2.4 and 2.5, the magnitude of the scattering vector $\vec{q}$ can be obtained; since

$$q^2 = |\vec{k}_f - \vec{k}_i|^2 = k_i^2 + k_f^2 - 2\vec{k}_i \cdot \vec{k}_f = 4k^2 \sin^2 \frac{\theta}{2}, \tag{2.6}$$

then

$$q = 2k \sin \frac{\theta}{2} = \frac{4\pi n_s}{\lambda} \sin \frac{\theta}{2}. \tag{2.7}$$

As shown in Eq. 2.3, the scattered field is a function of the component of the dielectric constant fluctuation tensor along the initial and final polarization directions and is independent of any specific laboratory coordinate system. However, it is convenient to use specific scattering geometries. The plane defined by the initial and final wave vectors of the light is called the scattering plane. It is necessary to define the scattering geometry in relation to the scattering plane. The geometry used in here is shown in Fig. 2.2.a. The scattering vector $\vec{q}$ is antiparallel to the X axis. In our experiment, both the incident light and the scattered light are polarized in the direction perpendicular to the scattering plane, as shown in Fig. 2.2.b.

2.2 Static Light Scattering

SLS measurements investigate the dependence of the average scattered intensity on the scattering angle. For small particles, SLS data can be analyzed to obtain the root mean-square radius of gyration $\langle R_g^2 \rangle^{1/2}$ and the molar mass of the particles. For large particles, more detailed information can be obtained. In this section, equations will be derived for light scattered from homogenous spherical particles.

2.2.1 Small particles

For a single small particle with polarizability α, the scattered intensity is independent of scattering angle and is given by [23]

$$\frac{I_s}{I_{inc}} = \left(\frac{2\pi n_s}{\lambda}\right)^4 \frac{\sin^2 \phi}{r^2} \alpha^2, \tag{2.8}$$

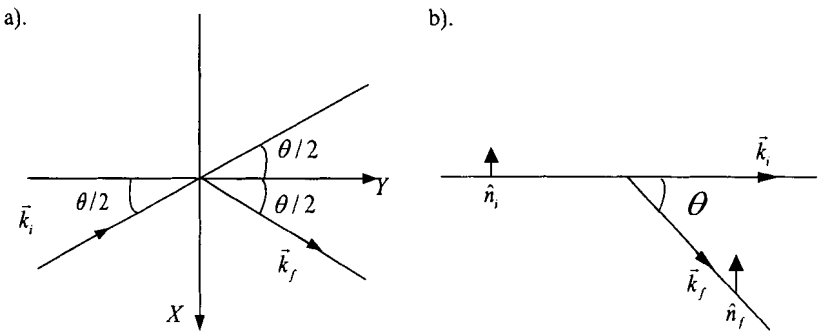

Figure 2.2: Scattering geometry and the polarization directions used in our light-scattering experiments. a. The scattering plane is the XY plane. The scattering angle is the angle between the wave vectors $\vec{k}_i$ and $\vec{k}_f$. b. The incident and scattered light. The polarized direction of incident light is out the scattering plane. The scattered light is measured in the vertical polarized direction.

where I_{inc} is the intensity of the incident beam, I_s is the intensity of the scattered light that reaches the detector, ϕ is the angle between the polarization of the incident electric field and the propagation direction of the scattered field, r is the distance between the scattering particles and the detector, λ is the wavelength of the incident light in vacuo and n_s is the solvent refractive index. In our measurements, ϕ is equal to 90^o.

The polarizability of the particles is related to the refractive index of the material. From the Lorentz-Lorenz equation [24]

$$4\pi\alpha N = \frac{3\left(n^2 - n_s^2\right)}{n^2 + 2n_s^2}, \tag{2.9}$$

where N represents the number of particles per cubic centimeter in the dispersion and n is the index of refraction. In dilute solutions, the refractive index is close to n_s. Then

$$4\pi\alpha N n_s^2 \approx n^2 - n_s^2. \tag{2.10}$$

We can expand n in a Taylor series in terms of the mass concentration c of particles in the dispersion. If all terms are neglected except the first two,

$$n = n_s + (dn/dc)\,|_{c=0} c \tag{2.11}$$

and, to first order in dn/dc,

$$n^2 = n_s^2 + 2n_s \left(dn/dc\right)|_{c=0} c. \tag{2.12}$$

Combining Eqs. 2.10 and 2.12, we have

$$\alpha = \frac{c\left(dn/dc\right)|_{c=0}}{2\pi N n_s} = \frac{M\left(dn/dc\right)|_{c=0}}{2\pi N_0 n_s}, \tag{2.13}$$

where M is the molar mass of particles and N_0 represents Avogadro's number. Using Eq. 2.13, the scattered intensity from a single particle can be written as

$$\frac{I_s}{I_{inc}} = \frac{4\pi^2 n_s^2 \left(dn/dc\right)^2|_{c=0} M^2}{N_0^2 \lambda^4 r^2} = \frac{KM^2}{r^2 N_0}, \tag{2.14}$$

where

$$K = \frac{4\pi^2 n_s^2 \left(dn/dc\right)^2|_{c=0}}{N_0 \lambda^4}. \tag{2.15}$$

The scattered intensity can thus be used to measure the molar mass if K is known.

2.2.2 Large Particles

If the particles are large, interference effects between light scattered at different points within a single particle must be considered. The scattered intensity for a single particle depends on scattering angle and can be written in terms of the form factor $P\left(q\right)$

$$\frac{I_s}{I_{inc}} = \frac{KM^2 P\left(q\right)}{r^2 N_0}. \tag{2.16}$$

The form factor $P\left(q\right)$ can be calculated under some conditions. As shown in Fig. 2.3, the wave vector is $\vec{k_i} = 2\pi n_s/\lambda \hat{n}$ inside the solvent and $\vec{k} = 2\pi n_p/\lambda \hat{n}$ inside a particle, where n_s and n_p are the refractive indices of the solvent and the particles and $\hat{n}$ is a unit vector of propagation, respectively. The smallest phase change that occurs as the field propagates between the planes 1 and 2 is $2\pi n_s R/\lambda$ inside the solvent and the largest phase change is $2\pi n_p R/\lambda$ inside the particle, here R is the radius of the particle. The largest phase difference between the light traversing the particle and the solvent is $4\pi\left(n_p - n_s\right)R/\lambda = 4\pi n_s\left(m-1\right)R/\lambda$, where m is n_p/n_s. In order to use the Rayleigh theory to calculate the scattered intensity, the phase difference on the planes that are perpendicular to the propagation vector must be small. A rough criterion is

$$\frac{4\pi n_s}{\lambda} R\left|m-1\right| \ll 1, \tag{2.17}$$

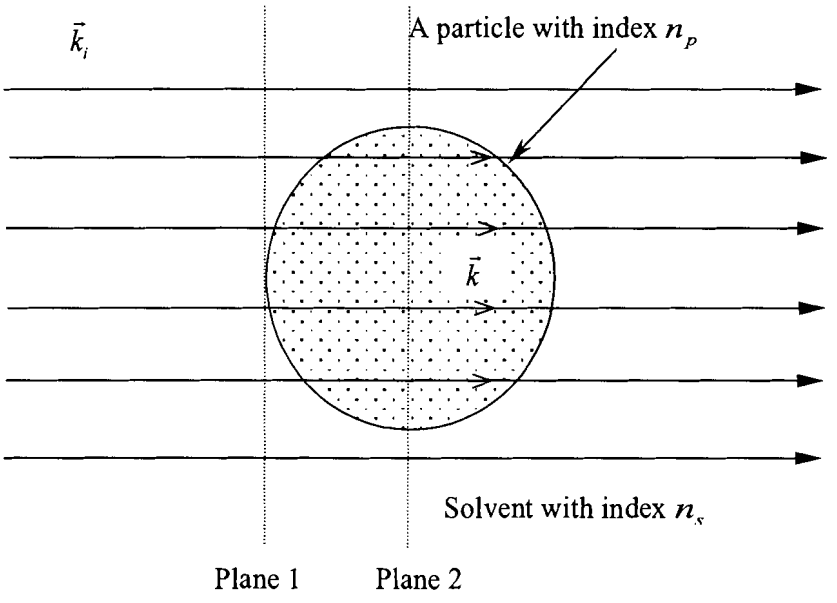

Figure 2.3: Schematic diagram showing the wave vectors inside and outside a particle.

where R is a characteristic dimension of a particle. This is known as the RGD condition. The criterion implies that the phase of a component of the wave traversing the particle is almost the same as the wave traversing the solvent and the effect of the particles on the phase of the local field can is small.

For homogeneous spherical particles where the RGD approximation is valid, the form factor $P(q, R_s)$ is given by [22]

$$P(q, R_s) = \frac{9}{q^6 R_s^6} \left(\sin(qR_s) - qR_s \cos(qR_s)\right)^2, \tag{2.18}$$

where R_s is the static radius of the particles. In the limit $qR_s \ll 1$,

$$P(q, R_s) \simeq 1 - \frac{1}{5} q^2 R_s^2 = 1 - \frac{1}{3} q^2 R_g^2, \tag{2.19}$$

where $R_g = \left(\frac{3}{5} R_s\right)^{1/2}$ is the radius of gyration of the particle.

If there are N particles in a unit volume, Eq. 2.16 can be written as

$$\frac{I_s}{I_{inc}} = \frac{KM^2P(q)}{r^2N_0}N. \tag{2.20}$$

The total number density thus can be written as

$$N = \frac{c \cdot N_0}{M}. \tag{2.21}$$

For large, noninteracting particles, the form factor can be written as $P(q) \approx 1 - \frac{1}{3}q^2\left\langle R_g^2\right\rangle$ [25]. So the Rayleigh ratio $R_{vv} = r^2\frac{I_s}{I_{inc}}$ can be written as

$$\frac{Kc}{R_{vv}} = \frac{1}{M}\left(1 + \frac{1}{3}q^2\left\langle R_g^2\right\rangle\right). \tag{2.22}$$

From a plot of $\frac{Kc}{R_{vv}}$ as a function of q^2, the $\left\langle R_g^2\right\rangle$ and M can be obtained. This is known as the Zimm plot analysis.

For a distribution of particles,

$$\frac{I_s}{I_{inc}} = \frac{K}{r^2N_0}\int_0^\infty M^2P(q, R_s)\,N(R_s)\,dR_s, \tag{2.23}$$

where $N(R_s)$ is the number density of particles of radius R_s and

$$\int_0^\infty N(R_s)\,dR_s = N, \tag{2.24}$$

where N is the total number density of particles. $N(R_s)$ can be written in terms of the particle number distribution

$$N(R_s) = NG(R_s), \tag{2.25}$$

where $\int G(R_s)\,dR_s = 1$. The molar mass of each size particle is $M = \frac{4\pi}{3}\rho R_s^3N_0$, so that the average molar mass can be defined as

$$\langle M(R_s)\rangle = \frac{4\pi}{3}\rho N_0\int R_s^3G(R_s)\,dR_s = \frac{4\pi}{3}\rho\left\langle R_s^3\right\rangle N_0, \tag{2.26}$$

where ρ is the density of particles. The total number density can be written as

$$N = \frac{c \cdot N_0}{\langle M\rangle}. \tag{2.27}$$

A new equation of the scattered intensity per unit volume for spherical particles can be written as

$$\begin{aligned}
\frac{I_s}{I_{inc}} &= \frac{K}{r^2 N_0}\int_0^\infty M^2 P(q,R_s)\,N(R_s)\,dR_s \\
&= \frac{K}{r^2 N_0}\int_0^\infty {N_0}^2\left(\frac{4}{3}\pi\rho\right)^2 R_s^6 P(q,R_s)\,NG(R_s)\,dR_s \\
&= \frac{K}{r^2 N_0}{N_0}^2\left(\frac{4}{3}\pi\rho\right)^2 N\int_0^\infty R_s^6 P(q,R_s)\,G(R_s)\,dR_s \\
&= \frac{Kc\langle M\rangle}{r^2}\frac{\int_0^\infty R_s^6 P(q,R_s)\,G(R_s)\,dR_s}{\left(\int_0^\infty R_s^3 G(R_s)\,dR_s\right)^2} \\
&= a\frac{\int_0^\infty R_s^6 P(q,R_s)\,G(R_s)\,dR_s}{\langle R_s^3\rangle},
\end{aligned} \tag{2.28}$$

where $a = K\frac{4\pi\rho c}{3r^2}N_0$.

When the values of qR_s are small, the form factor can be expanded according to Eq. 2.19, so that Eq. 2.28 can then be written as

$$\begin{aligned}
\frac{Kc}{\frac{r^2 I_s}{I_{inc}}} &= \frac{\left(\int_0^\infty R_s^3 G(R_s)\,dR_s\right)^2}{\langle M\rangle\int_0^\infty R_s^6 G(R_s)\,dR_s}\left(1+\frac{q^2\int_0^\infty R_s^8 G(R_s)\,dR_s}{5\int_0^\infty R_s^6 G(R_s)\,dR_s}+\cdots\right) \\
&= \frac{1}{M_{eff}}\left(1+\frac{1}{3}q^2\langle R_g^2\rangle\right),
\end{aligned} \tag{2.29}$$

where $\langle R_g^2\rangle$ is the mean-square radius of gyration of the macromolecule.
Comparing with the Zimm plot analysis, the mean square radius of gyration for a polydisperse system is

$$\langle R_g^2\rangle = \frac{3\int_0^\infty R_s^8 G(R_s)\,dR_s}{5\int_0^\infty R_s^6 G(R_s)\,dR_s} = \frac{3}{5}\frac{\langle R_s^8\rangle}{\langle R_s^6\rangle}, \tag{2.30}$$

which reduces to $\frac{\langle R_g^2 M^2\rangle}{\langle M^2\rangle}$ as derived by Pencer and Hallett [37]. The molar mass obtained from a Zimm plot analysis is

$$M_{eff} = \langle M\rangle\frac{\langle R_s^6\rangle}{\langle R_s^3\rangle^2}, \tag{2.31}$$

which reduces to $\frac{\langle M^2\rangle}{\langle M\rangle}$ as derived by van Zanten [38].

For homogeneous spherical particles, Equation 2.28 provides one method of relating size information to the average scattered light scattering intensity, when the RGD approximation is valid. Equation 2.30 provides the theoretical relationship between $\langle R_g^2\rangle$ and R_s and $G(R_s)$ when the Zimm plot analysis can be used.

2.2.3 Reflection Correction

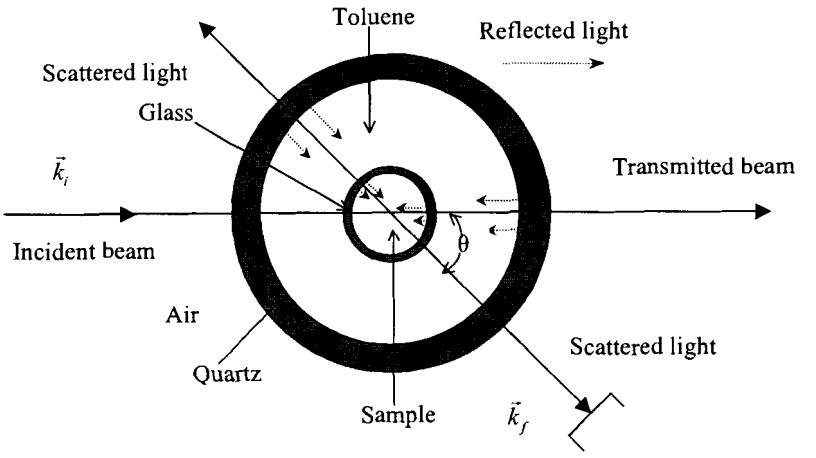

Figure 2.4: Schematic diagram showing the structure of the sample cell and vat where light is reflected. Dotted arrows represent reflected light, solid arrows represent incident, transmitted and scattered light.

As shown in Fig. 2.4, some scattered intensity detected comes from reflected light. There are two contributions. One is that the reflected light of the transmitted beam is scattered again at the scattering angle $\pi - \theta$ and the other is the scattered light of the incident beam at the scattering angle $\pi - \theta$ is reflected again if the signals are detected at a scattering angle θ. If reflected light is considered, the average scattered scattering intensity of a dilute polydisperse dispersion of spheres can be obtained for vertically polarized light:

$$\frac{I_s}{I_{inc}} = a\frac{\int_0^\infty R_s^6 P(q, R_s) G(R_s)\, dR_s + b\int_0^\infty R_s^6 P(q', R_s) G(R_s)\, dR_s}{\int_0^\infty R_s^3 G(R_s)\, dR_s}, \tag{2.32}$$

where

$$q' = \frac{4\pi}{\lambda} n_s \sin\frac{\pi - \theta}{2} \tag{2.33}$$

is the scattering vector of the reflected light, b is a constant with a value determined by the shape of the sample cell, the refractive indices of the solvent and the sample cell and the

geometry of the instrument.

Some scattered intensity comes from the reflected light, as shown in Fig. 2.4. There are four surfaces that reflect the transmitted or scattered light. The first is situated between the water and the glass sample cell; the second is located between the glass sample cell and the toluene; the third is between the toluene and the quartz and the fourth is between the quartz and the air. For each type of interface, the reflected light comes from two sources: one is the transmitted beam and the other is the reflected light of the scattered light at the scattering angle $\pi - \theta$ if the photon signals are measured at the scattering angle θ.
We can estimate the reflectivity coefficient from Fresnel's reflectivity coefficient. For the normal incidence, Fresnel's reflectivity coefficient is given by

$$R_{ref} = \frac{I_{ref}}{I_{inc}} = \left(\frac{n_2 - n_1}{n_2 + n_1}\right)^2, \tag{2.34}$$

where n_2 and n_1 are the refractive indices of the materials that form the surface where the reflection is occurring. If the refractive index n_2 is close to the refractive index n_1, Fresnel's reflectivity coefficient becomes very small.

In our experiments, the indices of toluene, water, air, glass and quartz are 1.49, 1.33, 1.00, 1.53 and 1.54 at normal temperature, pressure and a wavelength of 633 nm [32], respectively. The values of Fresnel's reflectivity coefficient for the four interfaces are listed in Table 2.1.

	First interface	Second interface	Third interface	Fourth interface
R_{ref}	0.005	0.0002	0.0003	0.045

Table 2.1: Fresnel's reflectivity coefficients of the four surfaces for normal incidence.

From the values of Fresnel's reflectivity coefficients at the four surfaces, it is apparent that the reflected light from the glass/toluene and toluene/quartz surfaces can be neglected. As shown in Fig. 2.4, each interface produces the reflected light from the two places, so the total Fresnel's reflectivity coefficient is about 10%.

2.3 Dynamic Light Scattering Theories

The DLS technique investigates the relationships between the normalized time autocorrelation function $g^{(2)}(\tau)$ and the delay time τ. The time dependence of scattered light is analyzed in terms of the time autocorrelation function $\langle I(t) I(t+\tau)\rangle$, where $I(t)$ and $I(t+\tau)$ are the scattered intensities of light at time t and $t+\tau$ and τ is the delay time [22]. Results are typically expressed in terms of the normalized time autocorrelation function $g^{(2)}(\tau)$

$$g^{(2)}(\tau) = \frac{\langle I(t) I(t+\tau)\rangle}{\langle I(t)\rangle^2}, \tag{2.35}$$

where the braces indicate averaging over time.

The time autocorrelation function of the scattered light intensity is related to the scattered field by [10]

$$\begin{aligned} \langle I(t) I(t+\tau)\rangle &= \left\langle |E(t)|^2 |E(t+\tau)|^2 \right\rangle \\ &= \left\langle |E(t)|^2 \right\rangle \left\langle |E(t+\tau)|^2 \right\rangle + \langle E(t) E^*(t+\tau)\rangle \langle E^*(t) E(t+\tau)\rangle \end{aligned} \tag{2.36}$$

where $E(t)$ and $E(t+\tau)$ are the scattered electric field of light at time t and $t+\tau$, respectively. Using the relations

$$\left\langle |E(t)|^2 \right\rangle = \left\langle |E(t+\tau)|^2 \right\rangle \tag{2.37}$$

and

$$\langle E(t) E^*(t+\tau)\rangle = \langle E^*(t) E(t+\tau)\rangle, \tag{2.38}$$

Eq. 2.36 can be written

$$\langle I(t) I(t+\tau)\rangle = \left\langle |E(t)|^2 \right\rangle^2 + \langle E(t) E^*(t+\tau)\rangle^2. \tag{2.39}$$

Using the normalized time autocorrelation function of the electric field of the scattered light $g^{(1)}(\tau)$,

$$g^{(1)}(\tau) = \frac{\langle E(t) E^*(t+\tau)\rangle}{\langle E(t) E^*(t)\rangle}, \tag{2.40}$$

the normalized intensity correlation function can be written

$$g^{(2)}(\tau) = 1 + \left(g^{(1)}(\tau)\right)^2. \tag{2.41}$$

This is known as the Siegert relation. To this point only the complex amplitude at a single point on the detector has been considered. In practice, large detector apertures are commonly used. The statistical consequences of spatial averaging over the detector apertures

must be calculated. For a typical continuous-wave gas laser, beam-intensity profiles are reasonably close to a Gaussian bell shape. The complex field or the intensity of scattered light is a stochastic process in space as well as in time. From the Siegert relation and considering the spatial dependence, one can write the normalized time autocorrelation function of the intensity of the scattered light $g^{(2)}(\tau)$ as [10]

$$g^{(2)}(\tau) = 1 + \beta \left[g^{(1)}(\tau) \right]^2, \tag{2.42}$$

where $\beta + 1$ is the value of the normalized time autocorrelation function of the intensity of the scattered light at a given scattering angle and zero delay time.

For a solution of noninteracting, monodisperse particles, $g^{(1)}(\tau)$ has the form

$$g^{(1)}(\tau) = \exp(-\Gamma\tau), \tag{2.43}$$

where $\Gamma = q^2 D$ is the decay rate, D is the macromolecular translational diffusion coefficient of the particles and q is the magnitude of the scattering vector.

For a polydisperse system, $g^{(1)}(\tau)$ consists of a distribution of exponentials

$$g^{(1)}(\tau) = \int_0^\infty G(\Gamma) e^{-\Gamma\tau} d\Gamma \tag{2.44}$$

where $G(\Gamma)$ is the normalized distribution of the decay rates.

The size distribution can be obtained using the method of moment analysis [[5] – [9]]. For this calculation, a mean decay rate $\bar{\Gamma}$ and the moments of the distribution μ_i are defined as

$$\bar{\Gamma} = \int_0^\infty \Gamma G(\Gamma) d\Gamma, \tag{2.45}$$

$$\mu_2 = \int (\Gamma - \bar{\Gamma})^2 G(\Gamma) d\Gamma, \tag{2.46}$$

$$\mu_3 = \int (\Gamma - \bar{\Gamma})^3 G(\Gamma) d\Gamma. \tag{2.47}$$

Assuming that $(\Gamma - \bar{\Gamma})\tau \ll 1$, one can write the exponential function in Eq. 2.44 as

$$\begin{aligned} \exp(-\Gamma\tau) &= \exp(-\bar{\Gamma}\tau) \exp\left[-(\Gamma - \bar{\Gamma})\tau\right] \\ &= \exp(-\bar{\Gamma}\tau) \left(1 - (\Gamma - \bar{\Gamma})\tau + \frac{(\Gamma - \bar{\Gamma})^2 \tau^2}{2!} - \frac{(\Gamma - \bar{\Gamma})^3 \tau^3}{3!} + \cdots \right) \end{aligned} \tag{2.48}$$

Substituting this expression into Eq. 2.44, we get

$$g^{(1)}(\tau) = \exp(-\bar{\Gamma}\tau) \left(1 + \frac{\mu_2 \tau^2}{2!} - \frac{\mu_3 \tau^3}{3!} + \cdots\cdots \right). \tag{2.49}$$

Then the intensity-intensity autocorrelation function can be written as

$$g^{(2)}(\tau) = 1 + \beta \exp\left(-2\bar{\Gamma}\tau\right)\left(1 + \frac{\mu_2\tau^2}{2!} - \frac{\mu_3\tau^3}{3!} + \cdots\cdots\right)^2. \tag{2.50}$$

Details of the particle size distribution can then be obtained by fitting Eq. 2.50 to the data.

The apparent hydrodynamic radius R_h is defined using the Stokes-Einstein relation

$$R_h = \frac{k_B T}{6\pi\eta_0 D}, \tag{2.51}$$

where η_0, k_B and T are the viscosity of the solvent, Boltzmann's constant and the absolute temperature. Equation 2.51 is obtained in the Stokes approximation for stick-boundary conditions [[22],[26]].

The width of the hydrodynamic radius distribution and the polydispersity index are defined as [27]

$$Width = \frac{\sqrt{\mu_2}}{\bar{\Gamma}} R_h \tag{2.52}$$

$$PD.I = \frac{\mu_2}{\bar{\Gamma}^2}. \tag{2.53}$$

2.4 Dimensionless Shape Parameter ρ

The results from SLS and DLS measurements can be used to infer details of particle shape. This is sometimes done by defining a dimensionless shape parameter for small particles

$$\rho = \left\langle R_g^2 \right\rangle^{1/2} / R_h. \tag{2.54}$$

For a long time, people have used that measurements of ρ to infer particle shapes [[2], [13] – [15]]. For a monodisperse model, theoretical values for different shapes of particles have been derived previously. For example, ρ is $\sqrt{3/5} \approx 0.775$ for homogenous spherical particles and ρ is $8/3\pi^{1/2} \approx 1.505$ [15] for linear chains. Since the static radius can be obtained from SLS directly, the parameter ρ will be discussed again in Chapter 5.1 and 5.2.5.

Chapter 3

Experiment

A light-scattering instrument built by ALV-Laser Vertriebsgesellschaft m.b.H (Langen, Germany) was used in our experiments. The samples that were studied included three commercial polystyrene latex samples and four Poly(N-isopropylacrylamide) microgel samples.

3.1 Instrument

A schematic diagram of the apparatus is shown in Fig. 3.1. A Uniphase 1145P He-Ne laser provides an incident polarized light beam with a power of 23 mW at a wavelength of 632.8 nm. The polarized light beam is focussed on the centre of the sample cell. In order to reduce the reflected light at the surface between the sample cell and the liquid, the glass cell is immersed in a cylindrical quartz vat containing toluene, a refractive index matching fluid. The light signals are detected by a photomultiplier tube after passing through the monitor. The 2.7 mm aperture cuts down the stray light. Pinhole 1 is located as close to the lens as possible. Both pinholes are 400 μm in diameter. The size of the pinholes was chosen as a compromise between the DLS and SLS techniques. The measurements of SLS need enough photons to obtain an average scattered intensity and the measurements of DLS require a small area to detect a coherent patch of light. The lens images the scattering volume onto the PMT. The lens and pinholes are installed in front of the Thorn EMI Electron Tube (Ruislip Middlesex, England, type: QL30F15RFI). The signals detected by the PMT are transferred to the computer. The detector arm including the detection optics and PMT can be moved to any scattering angle between 12^o and 150^o by a stepper motor. Combined with an ALV-LSE light scattering electronics unit, the ALV-5000 can provide records of laser

intensity, beam position and probe temperature.

The scattering intensity was recorded by the ALV-5000 Multiple Tau Digital Correlator. The ALV-5000 Multiple Tau Digital Correlator is a real-time computation correlator of photon correlation functions with a fixed range of simultaneous lag times between 0.2 μs and several hours.

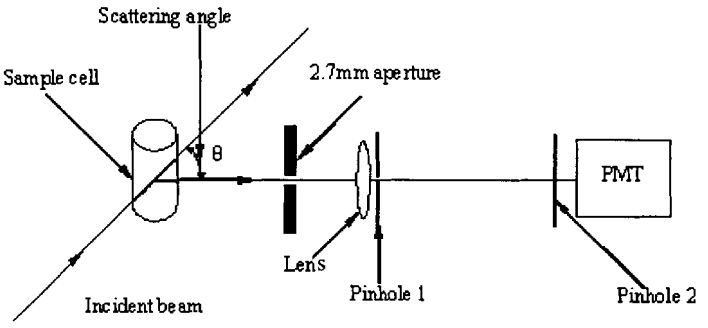

Figure 3.1: Schematic diagram showing the geometry of the detection system in the ALV laser light scattering setup.

3.2 Sample Preparation

3.2.1 Polystyrene Latex Spheres

Three standard polystyrene latex samples, obtained from Interfacial Dynamics Corporation (Portland, Oregon), were used in the SLS and DLS measurements. The sample names, product information and size information, including mean diameter and standard deviation, are shown in Table 3.1. Size information provided by the supplier was obtained using Transmission Electron Microscopy (TEM). Light scattering measurements were performed on dilute samples where the $PS-180$ was diluted to a weight factor 6.47×10^{-6}, the $PS-67$ was diluted to 1.02×10^{-5} and the $PS-110$ was diluted to 1.58×10^{-5}.

Sample Name	Product No.	Batch No.	Mean Radius(nm)	σ (nm)
$PS-180$	$2-200$	$817b$	90	2.5
$PS-67$	$1-60$	$511,3$	33.5	2.5
$PS-110$	$1-100$	$595,1$	55	2.5

Table 3.1: Information about the three polystyrene latex samples as provided by IDC.

3.2.2 Poly(N-isopropylacrylamide)(PNIPAM) Microgels

N-isopropylacrylamide was obtained from Acros Organics (Geel, Belgium) and was re-crystallized from hexane or acetone solutions. The structure of NIPAM is shown in Fig. 3.2. Potassium persulfate and N,N'-methylenebisacrylamide (BIS) were obtained from Aldrich and were used as received. The structures of the potassium persulfate and N,N'-methylenebisacrylamide are shown in Figs. 3.3 and 3.4, respectively. Fresh de-ionized water from a Milli-Q Plus water purification system (Millipore, Bedford, with a 0.2 μm filter) was used throughout the whole experiment. The synthesis of the four gel particles used in this work has been described elsewhere [[28],[29]].

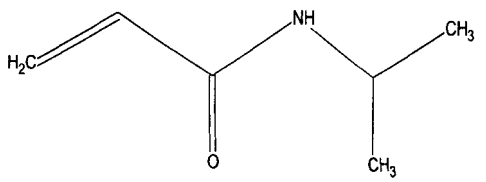

Figure 3.2: Structure of N-isopropylacrylamide.

All the four PNIPAM microgel samples were made using a precipitation polymerization technique. The simple process is that a solution 100 g including the PNIPAM monomers and the crosslinker N,N'-methylenebisaylamide was heated to a temperature of 70°C and potassium persulfate (KPS, 40 mg) was introduced to initiate polymerization. The total weight of the PNIPAM monomers and the crosslinker N,N'-methylenebisaylamide is 1 g. The reaction system was stirred at 70°C for about 4 hours. The solution was then cooled to room temperature

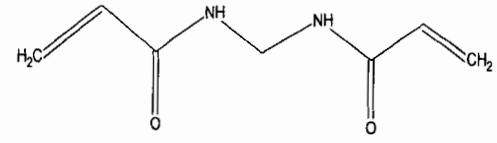

Figure 3.3: Structure of N, N'- methylene bisacrylamide.

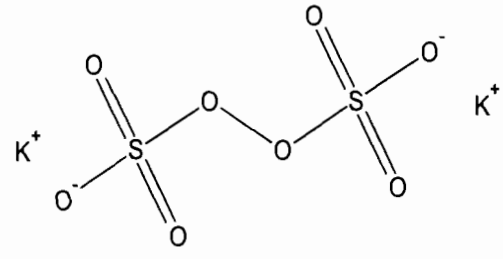

Figure 3.4: Structure of potassium persulfate.

The four samples were named according to the molar ratios n_{BIS}/n_{NIPAM} of N, N'-methylenebisacrylamide over N-isopropylacrylamide. They were centrifuged at 14,500 RPM followed by decantation of the supernatant and re-dispersion four times to remove free ions and any possible linear chains. Then the samples were diluted for light scattering to weight factors of 5.9×10^{-5}, 8.56×10^{-6}, 9.99×10^{-6} and 8.38×10^{-6} for $PNIPAM - 0$, $PNIPAM - 1$, $PNIPAM - 2$ and $PNIPAM - 5$, respectively. Before the measurements were made, $PNIPAM - 1$, $PNIPAM - 2$ and $PNIPAM - 5$ were filtered using 0.45 μm filters (Millipore, Bedford), respectively. Due to the large size of $PNIPAM - 0$, it was used directly.

3.3 Experimental Measurements

The ALV-5000 Multiple Tau Digital Correlator program records the autocorrelation function of the intensity of the scattered light $g^{(2)}(\tau)$, the standard deviations of this function, temperature, viscosity, refractive index, wavelength, scattering angle and measurement time. Measurements were performed five times at each angle for all samples except the $PNIPAM - 0$ sample, in which measurements were performed only twice. The time autocorrelation function of the scattered light intensity $g^{(2)}(\tau)$ is characterized by the decay time constant τ_c. It measures the Brownian motion of colloidal particles in dispersion. In order to obtain accurate statistical results of measurements, the measurement time must be greatly larger than the decay time constant. The relationship between the measurement time and the required accuracy is given out in the following discussion.

For DLS, the experimental uncertainty $\Delta\Gamma$ of the decay rate Γ is determined by the measurement time t, as is given by

$$\frac{\Delta\Gamma}{\Gamma} = 4\sqrt{\frac{\tau_c}{t}}, \tag{3.1}$$

where $\frac{\Delta\Gamma}{\Gamma}$ is the precision that measurements are required. For all the experimental data, the measurement time was set to obtain a precision of 1%.

For SLS, experimental uncertainty depends on the uncertainty in the scattered intensity $\frac{1}{N_s}$ and the uncertainty due to intensity fluctuation $\frac{1}{N_c}$, where $N_c = \frac{t}{\tau_c}$ as given by [30]

$$\frac{\sigma_S^2}{S^2} = \frac{1}{N_s} + \frac{2\tau_c}{t}\frac{\langle \delta P^2 \rangle}{\langle P \rangle^2}, \tag{3.2}$$

where N_s is the mean number of counts in time t obtained from the scattered intensity and the transmitted power, S is the ratio of the scattered to transmitted power and σ_S^2 is its variance, and P is the scattered power and δP is its fluctuation amplitude. The values of $\frac{\langle \delta P^2 \rangle}{\langle P \rangle^2}$ depend on the collection and focusing geometries. In our measurements, the mean number of counts N_s is usually very large and $\frac{\langle \delta P^2 \rangle}{\langle P \rangle^2}$ approximates 0.4, so Eq. 3.2 can be written as

$$\frac{\sigma_S^2}{S^2} = \frac{0.8\tau_c}{t}. \tag{3.3}$$

For the static scattered light intensity, the data collection program records the scattering vector, count rate, monitor intensity, temperature and the standard deviation of these quantities. In order to estimate an experimental uncertainty, each run was performed 3

times; The duration of each measurement was determined using Eq. 3.3 and the limit for the standard deviation of the measured intensity of all runs performed at one angle was set to be 5%. If 5% is exceeded, the measurement is repeated at the same angle using the same parameters.

Chapter 4

Data Analysis and Results

In this Chapter, the theoretical models described in Chapter 2 will be used to analyze the SLS and DLS experimental data to obtain information about the size and polydispersity of the samples.

4.1 Static Light Scattering Data Analysis

From the theoretical analysis in Chapter 2, size distributions for homogenous spherical particles can be obtained by considering the relationship between I_s/I_{inc} and q. In order to obtain the size distribution $G(R_s)$ from the SLS data, the model of particle size distribution in Eq. 2.28 must be determined. Various probability distributions have been used to describe particle size distribution. For example, Bryant *et al* [11] used three model distributions (Gaussian, Log-normal and Weibull) to describe both static and dynamic scattering data from homogenous spherical particles. Of these distributions, Gaussian or normal error distribution is the most important in the statistical analyses of data because, in practice, it appears to describe the distribution for many experiments [31]. When we investigated the SLS data, the Gaussian distribution was chosen first to describe our data. Since the fitting results were very good, the Gaussian distribution was subsequently used to investigate our experimental data. It is written as

$$G(R_s; \langle R_s \rangle, \sigma) = \frac{1}{\sigma\sqrt{2\pi}} \exp\left[-\frac{1}{2}\left(\frac{R_s - \langle R_s \rangle}{\sigma}\right)^2\right], \tag{4.1}$$

where $\langle R_s \rangle$ is the mean static radius and σ is the standard deviation.

For monodisperse systems, Eq. 2.28 can be written as

$$\frac{I_s}{I_{inc}} = aR_s^3 P(q, R_s) = \frac{9a\left[\sin(qR_s) - qR_s\cos(qR_s)\right]^2}{q^6 R_s^3}. \tag{4.2}$$

If a sample consists of homogenous spherical particles, the mean static radius can be obtained approximately using Eq. 4.2.

4.1.1 Zimm Analysis and Results

At small scattering angles, where qR_s is small, the spherical form factor can be approximated by Eq. 2.19. The exact values, A, and approximate values ,B, of the spherical form factor and the relative deviation $(A-B)/A$ are shown in Fig. 4.1 for small values of qR_s. At $qR_s = 1$, the deviation is only 2%.

In this situation, the Zimm plot can be used to obtain the approximate values of $\langle R_g^2\rangle^{1/2}$ using $\frac{Kc}{R_{vv}}$ as a linear function of q^2. For example, Fig. 4.2 shows the data of $\frac{Kc}{R_{vv}}$ taken over the entire angular range for $PS-180$. The function between $\frac{Kc}{R_{vv}}$ and q^2 is linear for $q^2 < 1.2\times10^{-4}\ nm^{-2}$. From the slope, $\langle R_g^2\rangle^{1/2} = 69.1\ nm$, corresponding to $qR_s = 0.97$ at the largest q included in this fit.

The results of $\langle R_g^2\rangle^{1/2}_{Zimm}$ for the polystyrene latex samples and PNIPAM samples with small particle sizes at high temperatures are shown in Table 4.1 and 4.2, respectively.

Sample	$\langle R_g^2\rangle^{1/2}_{Zimm}\ (nm)$
$PS-67$	27.0 ± 0.5
$PS-110$	46.8 ± 0.3
$PS-180$	$69.\pm2.0$

Table 4.1: Values of $\langle R_g^2\rangle^{1/2}_{Zimm}$ for the PS samples.

4.1.2 Fitting the Form Factor to the Data and Results

4.1.2.1 Polystyrene Latex Sphere Data and Results

Since the distributions of the polystyrene latex particles are very narrow and the sizes are small, Eq. 4.2 is a good method to obtain the mean size of the polystyrene latex particles. The experimental data and fit results for $PS-180$ are shown in Fig. 4.3. Here, a good fit

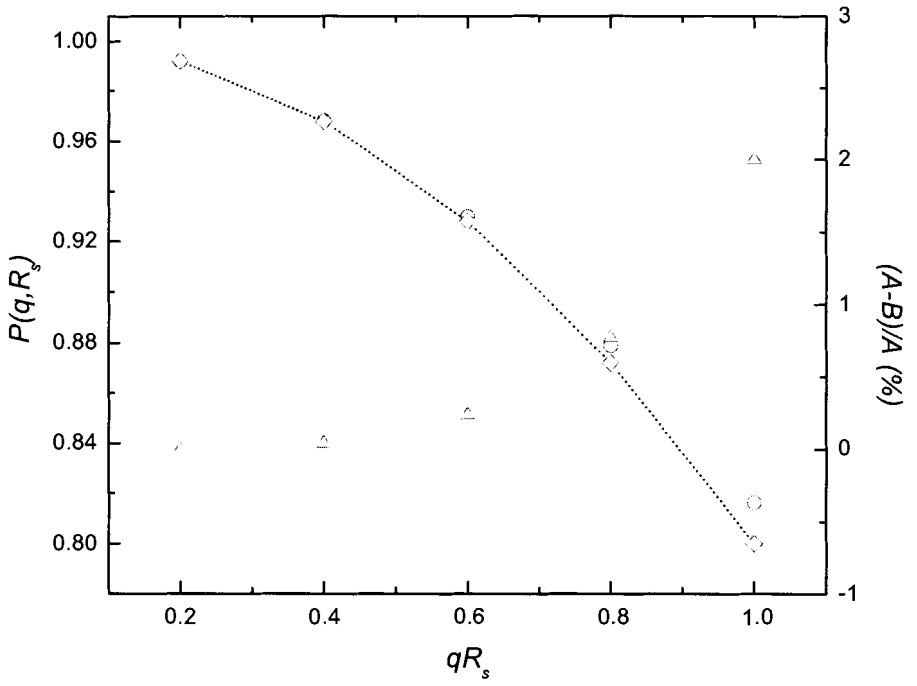

Figure 4.1: The exact values A and approximate values B of the spherical form factor. $\circ$ shows the exact values, $\diamond$ represents the approximate values and $\triangle$ shows the relative deviations $(A - B)/A$.

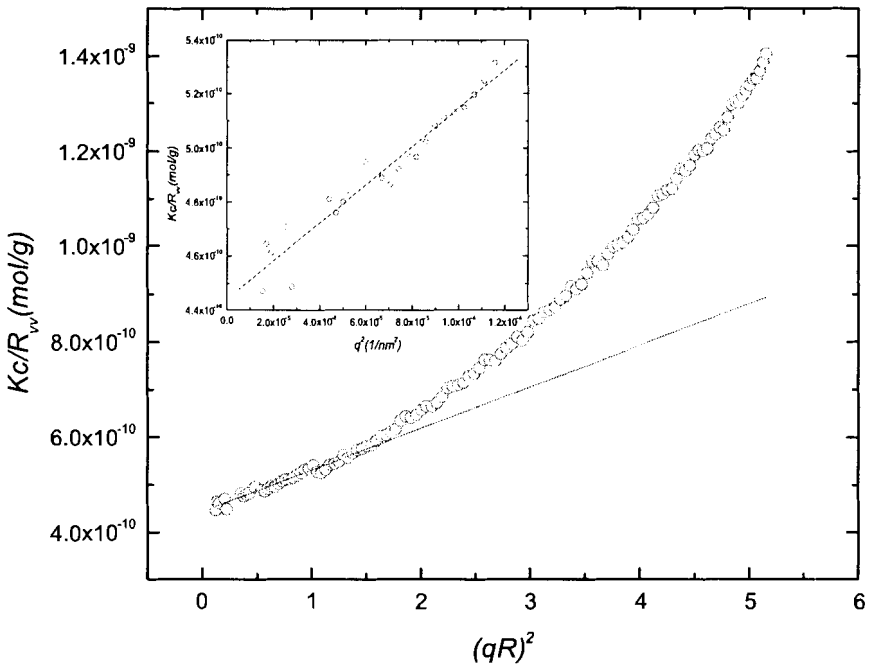

Figure 4.2: The results of the Zimm plot analysis and the experimental data for $PS - 180$ over the entire scattering vector range. The circles show the experimental data and the line shows the results of the Zimm plot obtained in a small scattering vector range plotted as a function of qR^2 where $R = 90nm$. The results of a Zimm plot obtained in a small scattering vector range are shown in the inset. The circles show the experimental data, and the line shows a linear fit to the plot of Kc/R_{vv} as a function of q^2.

Sample(Temperature)	$\langle R_g^2 \rangle_{Zimm}^{1/2} (nm)$
$PNIPAM - 5\ (40^o)$	$116. \pm 3.$
$PNIPAM - 2\ (40^o)$	$96. \pm 5.$
$PNIPAM - 1\ (40^o)$	$97. \pm 5.$
$PNIPAM - 0\ (40^o)$	$81. \pm 2.$
$PNIPAM - 0\ (34^o)$	$105. \pm 3.$

Table 4.2: Values of $\langle R_g^2 \rangle_{Zimm}^{1/2}$ for the PNIPAM samples.

over the whole q-range was obtained, with no systematic residuals. The residual is defined as $(y_i - y_{fit})/\sigma_i$ for the ith data point, where y_i is the experimental value, y_{fit} is the fit value and σ_i is the error of the ith data point.

For the three polystyrene samples, the results of static radii and χ^2 are listed in Table 4.3.

Sample	$\langle R_s \rangle\ (nm)$	χ^2
$PS - 67$	33.3 ± 0.2	9.69
$PS - 110$	56.77 ± 0.04	9.19
$PS - 180$	92.05 ± 0.05	12.10

Table 4.3: The fit results for the polystyrene samples.

4.1.2.2 Poly(N-isopropylacrylamide)(PNIPAM) Microgel data and Results

In general, any particle system has a particle-size distribution and the monodisperse model is only an ideal case. In order to obtain the size distribution, we use Eqs. 2.28 and 4.1 to fit the measured static data.

The data for $PNIPAM - 5$ are plotted in Fig. 4.4. The values of I_s/I_{inc} show one minimum. From Eq. 2.18, the value of qR_s at the minimum is 4.493. For this data, the value of the scattering vector at the minimum of the scattered intensity is about 0.0207 nm^{-1}, corresponding to a radius of 217 nm.

A nonlinear least squares fitting program was used to obtain the size information from SLS. In the method of least squares, the hypothesis is that for a set of data the optimum description is one that minimizes the weighted sum of the squares of the deviation of the

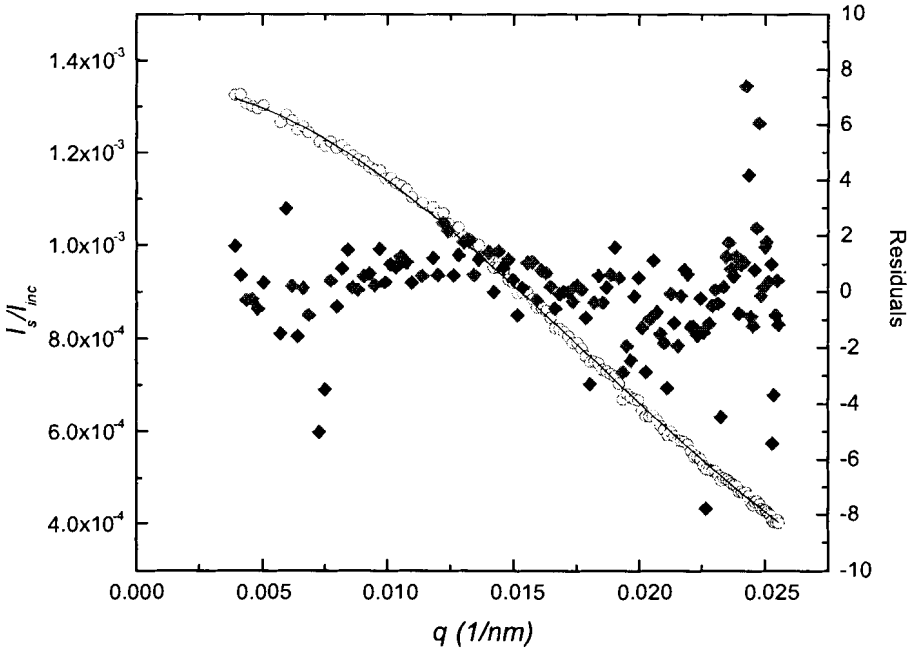

Figure 4.3: The experimental data and fit results for $PS - 180$. The circles show the experimental data, the line shows the results of fitting Eq. 4.3 to the data and the diamonds show the residuals.

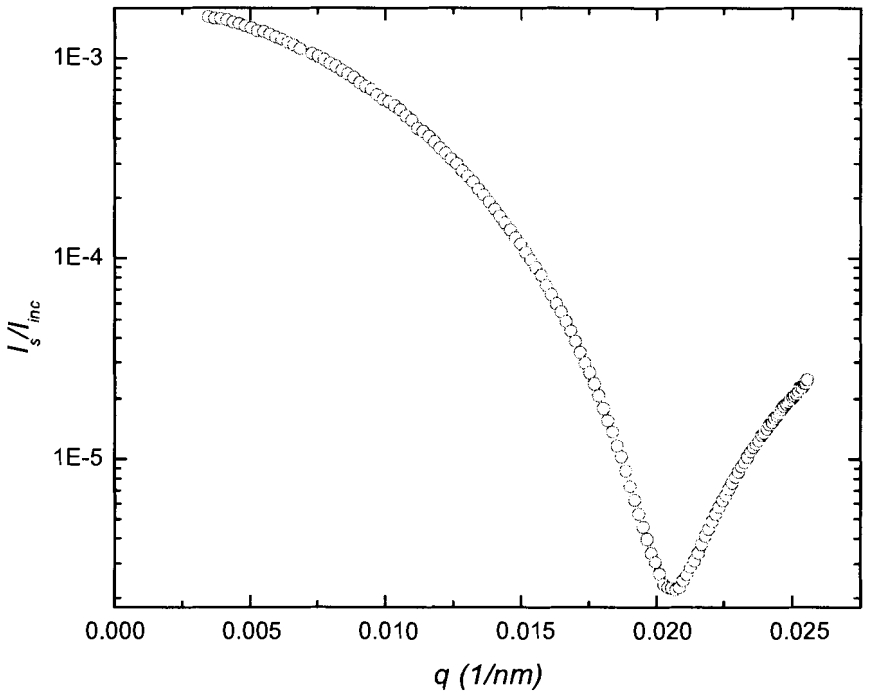

Figure 4.4: All the experimental data for $PNIPAM - 5$, plotted as a function of q.

data from the fitting function. For a function $y(x)$ fit to N data points, the statistic χ^2 is defined as

$$\chi^2 = \frac{1}{N-n} \sum_{i=1}^{N} \left(\frac{y_i - y_{fit}}{\sigma_i} \right)^2, \tag{4.3}$$

where n is the number of parameters, y_i is the measured value at the ith datum, σ_i are the uncertainty relative to the ith datum and y_{fit} is the value of the model function at the ith datum.

In order to fit Eq. 2.28 to the data, one must assume a probability distribution of particle sizes. The values of χ^2 are used to test the fit. If the distribution is a good approximation of the particle size distribution, the value of χ^2 should approximate unity. In general, if the values of χ^2 are reasonably probable, the assumed probability distribution can be trusted. For the results of χ^2 are much larger than 1, this shows that maybe an incorrect probability distribution was chosen or a poor measurement was obtained or small uncertainties were obtained. For very small values, in general, it imply some misunderstanding of the experiment [31].

In practice, we first consider whether the theoretical values are consistent with the experimental data when the fit results are obtained. If the fit results are consistent with the experimental data, the values of the residuals and χ^2 will be considered next. If the residuals show systematic variance or if χ^2 is large, the reasons will need to be studied further. In general, we need to consider the model again if this situation is met.

When Eq. 2.28 was fit to this data, it was found that the results for the mean static radii $\langle R_s \rangle$ and standard deviation σ depended on the angular range being fit, as listed in Table 4.4. If a small angular range is chosen, the parameters are not well-determined. As the angular range is increased, χ^2 and the uncertainties in the parameters decrease and $\langle R_s \rangle$ and σ stabilize. If the fitting angular range continues to increase, the values of $\langle R_s \rangle$ and σ begin to change and χ^2 grows. It is apparent that Eqs. 2.28 and 4.1 cannot be used to describe the data in the vicinity of the intensity minimum which lies at about 103^o. Other features of particles, for example, deviations of the particle number distribution from a Gaussian distribution, deviations of the particle shape from a perfect sphere, deviations of the density of particles from homogeneity as well as experimental concerns such as light scattered from the solvent, the contribution of reflected light, etc., can affect the scattered intensity, especially near the minimum.

Angular range	$\langle R_s \rangle (nm)$	$\sigma(nm)$	χ^2
15^o to 40^o	189.92 ± 30.58	38.12 ± 15.69	1.44
15^o to 50^o	199.50 ± 10.45	32.84 ± 6.49	1.17
15^o to 60^o	210.80 ± 2.39	24.66 ± 2.29	1.03
15^o to 65^o	215.47 ± 1.47	19.91 ± 1.87	1.07
15^o to 70^o	216.94 ± 0.60	18.10 ± 1.02	1.06
15^o to 75^o	216.69 ± 0.40	18.46 ± 0.71	1.07
15^o to 80^o	216.71 ± 0.25	18.33 ± 0.50	1.07
15^o to 85^o	217.55 ± 0.14	16.73 ± 0.36	1.23
15^o to 90^o	217.98 ± 0.09	15.66 ± 0.27	1.51
15^o to 95^o	218.14 ± 0.06	14.57 ± 0.17	2.49
15^o to 100^o	218.19 ± 0.07	14.42 ± 0.17	3.58

Table 4.4: The fit results for the data shown in Fig. 4.4 for different angular ranges.

To consider the effects of reflected light, we fit Eq. 2.32 to the data of Fig. 4.4 for various factors of reflected light b. The fit results are listed in Table 4.5, and the results for $b = 0.011$ are shown in Fig. 4.5. The values of χ^2 are large and the residuals contain systematic variations.

b	$\langle R_s \rangle (nm)$	$\sigma\,(nm)$	χ^2
0.009	217.6 ± 0.3	9.4 ± 0.6	91.75
0.010	217.1 ± 0.2	9.3 ± 0.6	70.46
0.011	216.7 ± 0.2	9.2 ± 0.6	65.53
0.012	216.3 ± 0.2	9.1 ± 0.6	75.34
0.013	215.9 ± 0.3	9.0 ± 0.7	98.25
0.014	215.5 ± 0.3	8.8 ± 0.9	132.82

Table 4.5: Fit results for $PNIPAM - 5$ obtained from Eq. 2.32 using various values of b.

If the data in the vicinity of the intensity minimum are neglected, a much better fit is obtained. Table 4.6 lists results for fits to the data excluding the range from 0.01781 to 0.02435 nm^{-1}. The values obtained at b=0.011 where χ^2 is minimum are consistent with the results obtained using Eq. 2.28 over the fitting range between 15^o and 80^o. b have a large difference with the calculated values of the total Fresnel's reflectivity coefficient 0.1 because the shapes of our sample cell and the vat are cylindrical.

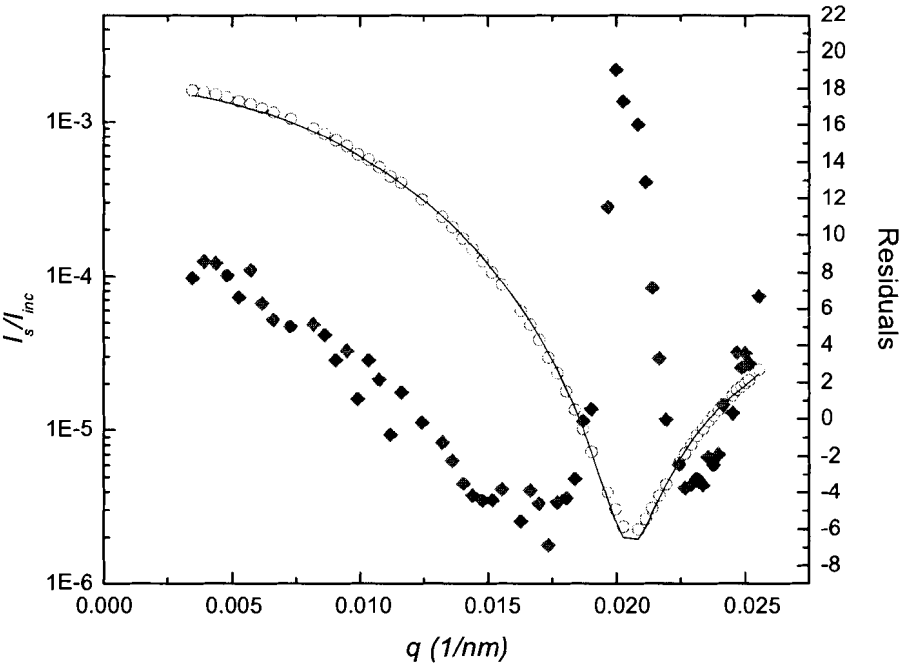

Figure 4.5: The experimental data measured at a temperature of 29°C and fit results using Eq. 2.32 for $PNIPAM-5$ over the entire angular range. The circles show the experimental data; the line shows the fit results; and the diamonds show the residuals.

b	$\langle R_s \rangle (nm)$	$\sigma (nm)$	χ^2
0.009	220.3 ± 0.2	$8. \pm 2.$	10.84
0.010	218.76 ± 0.01	14.0 ± 0.4	2.88
0.011	216.9 ± 0.1	18.2 ± 0.4	1.88
0.012	215.1 ± 0.3	21.5 ± 0.8	9.03
0.013	213.3 ± 0.6	$24. \pm 1.$	25.54
0.014	$212. \pm 1.$	$27 \pm 2.$	52.22

Table 4.6: The fit results for $PNIPAM - 5$ obtained by using Eq. 2.32 and neglecting experimental data near the intensity minimum.

One possible explanation for the deviation of the fit of Eq. 2.32 to the data near the minimum is that the number distribution deviates from a Gaussian. The results obtained using Eq. 2.28 over the fitting range from 15 to 80^o were used to calculate the expected values of I_s/I_{inc} in the entire scattering angular range. First a full Gaussian was considered and the values of fit results were input to Eq. 2.28. Next, a truncated Gaussian was used, ie. integrated between $\langle R_s \rangle \pm 1.2\sigma$ instead of between 1 and 800 nm, and the fit values were still input to Eq. 2.28. Finally, the integrated range is same with the second, the values were input to Eq. 2.32. All results are shown in Fig. 4.6. The expected results in the last situation are consistent with the experimental data. The results also show that the SLS data are very sensitive to the particle size distribution. This conclusion has some difference with Bryant's [11] results. Since Bryant did not give the values of χ^2, the results cannot be compared directly.

Because the fit values of the mean static radius and standard deviation for $PNIPAM-5$ in the scattering range between 15^o and 80^o stabilize and fits to this range yield results consistent with the location of the first minimum, the fit results for this scattering angle range are used to provide size information for $PNIPAM-5$ at a temperature of 29°C. The fit results and the residuals in the angular range 15^o to 80^o are shown in Fig. 4.7.

Because of the temperature sensitivity of the PNIPAM samples, their sizes decrease as temperature increases and the minimum of scattered intensity is no longer measured on our apparatus. For the experimental data of $PNIPAM - 5$ measured at a temperature of 40°C, the static radii $\langle R_s \rangle$ and standard deviations σ found for fitting different angular ranges are listed in Table 4.7. If a small angular range is chosen, the parameters are not well-determined. As the angular range is increased, the uncertainties in the parameters

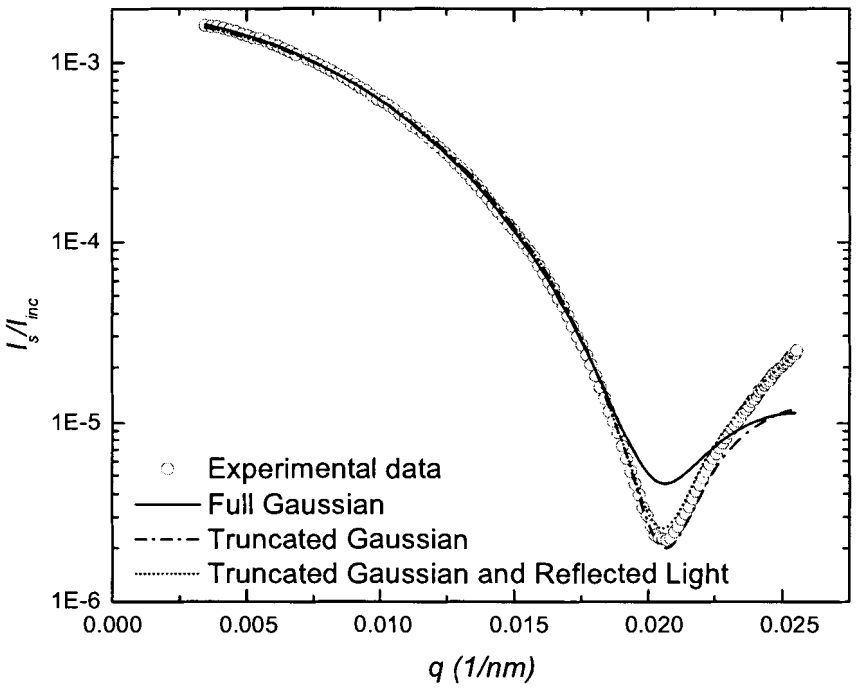

Figure 4.6: The experimental data and the calculated values for $PNIPAM - 5$ over the entire angular range. First the line shows the calculated results of the incident light calculated during full distribution; Second,the dash dot represents the calculated results of the incident light calculated between $\langle R_s \rangle - 1.2\sigma$ and $\langle R_s \rangle + 1.2\sigma$ and third, the short dot shows the calculated values of the incident and the reflected light calculated between $\langle R_s \rangle - 1.2\sigma$ and $\langle R_s \rangle + 1.2\sigma$ with b: 0.011.

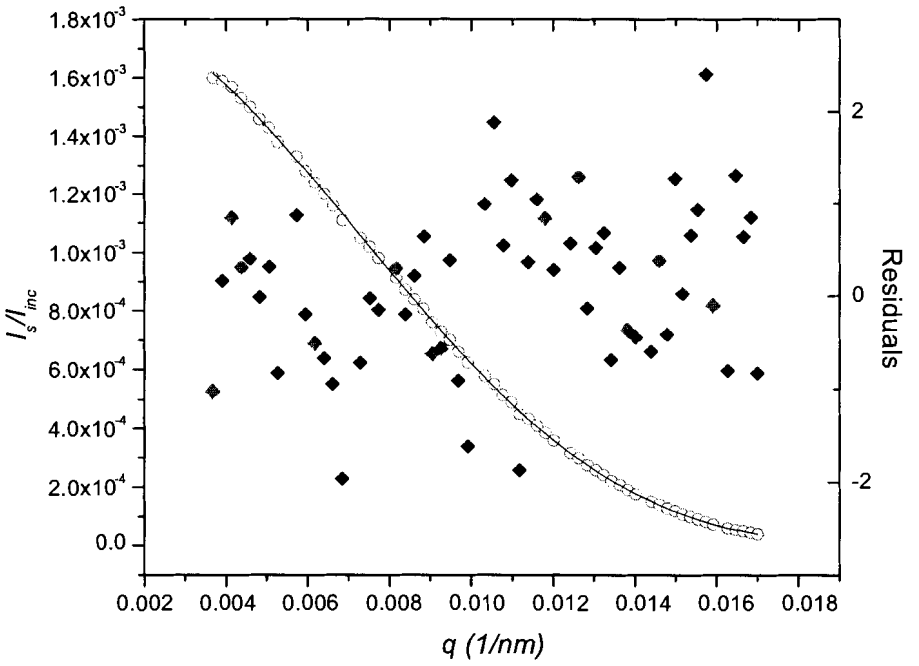

Figure 4.7: The experimental and fit results for $PNIPAM - 5$ measured at a temperature of 29°C. The circles show the experimental data, the line shows the fit results and the diamonds show the residuals.

decrease and $\langle R_s \rangle$ and σ stabilizes. The fit results over the entire angular range are shown in Fig. 4.8. The fit results over the entire scattering angular range are chosen to be the particle size distribution obtained using the SLS technique since $\langle R_s \rangle$ and σ stabilize.

Angular range	$\langle R_s \rangle (nm)$	$\sigma (nm)$	χ^2
15^o to 65^o	143.78 ± 8.34	7.32 ± 14.78	2.68
15^o to 75^o	116.70 ± 7.35	27.01 ± 3.40	2.97
15^o to 85^o	130.01 ± 3.54	19.45 ± 2.41	2.92
15^o to 95^o	142.29 ± 2.33	7.26 ± 4.48	4.43
15^o to 105^o	138.18 ± 1.50	13.47 ± 1.57	3.97
15^o to 125^o	142.30 ± 0.57	7.97 ± 1.22	3.18
15^o to 135^o	140.09 ± 0.46	11.59 ± 0.73	3.66
15^o to 145^o	139.57 ± 0.41	12.33 ± 0.63	3.87
15^o to 150^o	139.34 ± 0.31	12.36 ± 0.55	5.50

Table 4.7: The fit results for $PNIPAM - 5$ at different angular ranges at a temperature of 40^oC.

The fit results are consistent with that the shapes of our PNIPAM samples are spherical. The result is the same as other authors. Pelton [16] investigated PNIPAM samples using the transmission electron micrograph and the scanning electron micrograph and Kratz et al ([18], [33]) using the scanning electron micrograph to show the particle shape. All pictures show that the shapes of the PNIPAM microgel particles are spherical.

The same fit procedure was applied for all the data of the PNIPAM samples at all temperatures; the fit static radii $\langle R_s \rangle$ and standard deviations σ are listed in Appendix A.

The fit results for the four PNIPAM microgel samples show an interesting result that the value of $\sigma / \langle R_s \rangle$ is about 10% both below and above the phase transition. If the distribution is assumed to be a constant between 0 and R_{max}, the value of $\sigma / \langle R \rangle$ will be $\sqrt{1/3}$. If it is in proportion to $1/R_s$ between R_{min} and R_{max}, the value of $\sigma / \langle R \rangle$ will be $(ln(R_{max}/R_{min})/2 - 1)^{1/2}$ for $R_{min} \ll R_{max}$. The expected values of $\sigma / \langle R \rangle$ are large differences with those obtained fitting the SLS data for PNIPAM microgel samples. To the distributions of PNIPAM microgel samples, they are determined by the method of microgel synthesis called precipitation polymerization [16]. The simple polymerization procedure can produce remarkably uniform particles.

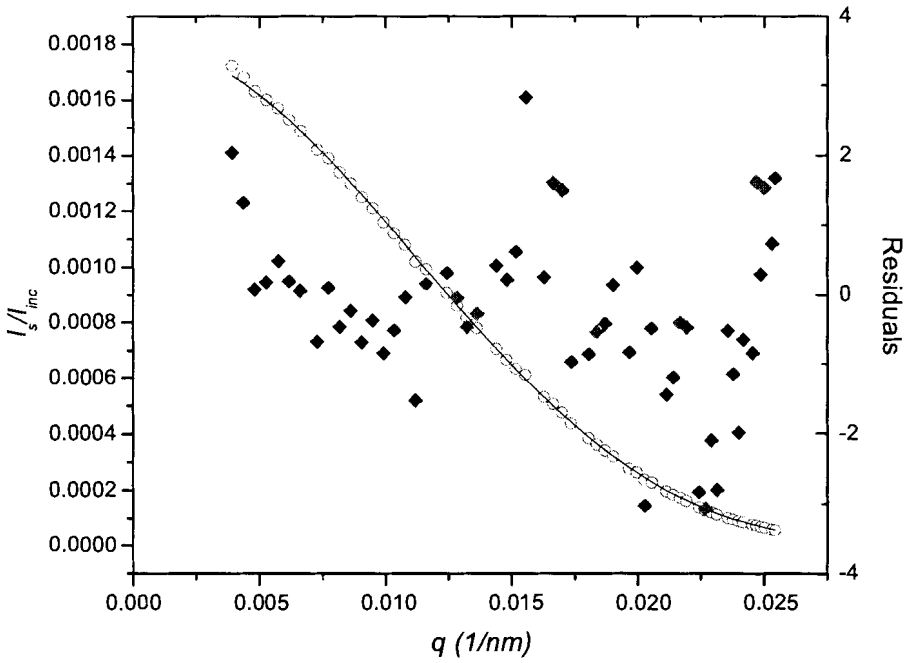

Figure 4.8: The experimental and fit results for $PNIPAM - 5$ measured at a temperature of 40°C. The circles show the experimental data, the line shows the fit results and the diamonds show the residuals.

4.2 Dynamic Light Scattering Data Analysis and Results

In general, the size information from DLS data is obtained using moment analysis or the inverse Laplace transform. Both methods analyze the autocorrelation function of the scattered light intensity $g^{(2)}(\tau)$ that can be measured using the ALV-5000 Multiple Tau Digital Correlator. In this section, moment analysis is used to obtain size information. For monodisperse particles only the first moment is included in the fit. For polydisperse particles, more moments must be included; in our case only the addition of the second moment was required.

4.2.1 Polystyrene Latex Spheres data and Results

The intensity-intensity correlation function measured for $PS-67$ at 90^o is shown in Figs. 4.9 and 4.10 for $\mu_2 = 0$ and $\mu_2 \neq 0$ respectively. Figure 4.9 shows the autocorrelation function of the light scattered intensity $g^{(2)}(\tau)$ and a fit of Eq. 2.50 to the data with $\mu_2 = 0$ during the delay time range 10^{-6} to 7.168×10^{-4} s. The criterion for data cutoff is $g^{(2)}(\tau) - 1 < 0.01$. The residuals vary randomly as the delay time is changed. Figure 4.10 shows the same data with a fit of Eq. 2.50 with $\mu_2 \neq 0$. The residuals are also random.

Pairs of fit results for five independent data sets are listed in Table 4.8 for the scattering angle 90^o. The results obtained for μ_2 often are negative, which is in contradiction to its definition.

	Γ_{first}	μ_2	χ^2	Γ_{two}	μ_2	χ^2
1	$4610. \pm 20.$	0	0.40	$4550. \pm 40.$	$(-18. \pm 9.) \times 10^4$	0.35
2	$4600. \pm 20.$	0	0.43	$4640. \pm 40.$	$(1. \pm 1.) \times 10^5$	0.42
3	$4590. \pm 20.$	0	0.32	$4590. \pm 40.$	$(-0.2 \pm 9.) \times 10^4$	0.33
4	$4630. \pm 20.$	0	0.42	$4600. \pm 40.$	$(-9. \pm 9.) \times 10^4$	0.41
5	$4600. \pm 20.$	0	0.46	$4570. \pm 40.$	$(-10. \pm 9.) \times 10^4$	0.45

Table 4.8: The fit results for $PS - 67$ at a scattering angle of 90^o.

Figure 4.11 shows the autocorrelation function of the scattered light intensity $g^{(2)}(\tau)$ for $PS - 67$ at a scattering angle of 30^o. Equation 2.50 was fit to the data with $\mu_2 = 0$. The residuals show systematic variations with the delay time. Figure 4.12 show the same data with a fit of Eq. 2.50 with $\mu_2 \neq 0$. Again, the residuals show systematic variations.

Fit results obtained using both procedures are listed in Table 4.9 for five independent

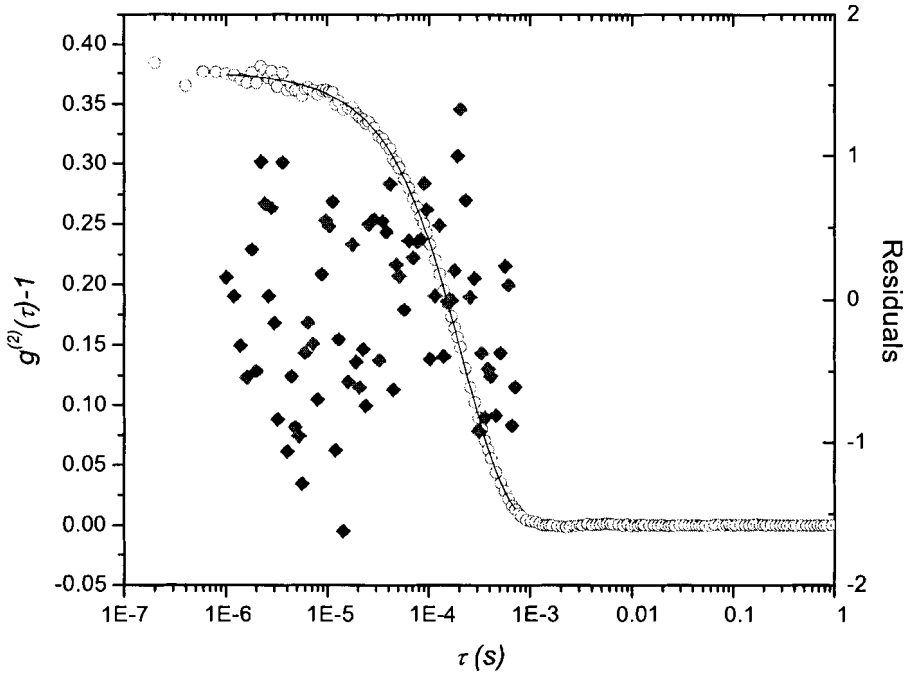

Figure 4.9: The autocorrelation function of the scattered light intensity $g^{(2)}(\tau) - 1$ for $PS - 67$ measured at a scattering angle of 90^o. The circles show the experimental data, the line shows the fit results for $\mu_2 = 0$ and the diamonds show the residuals.

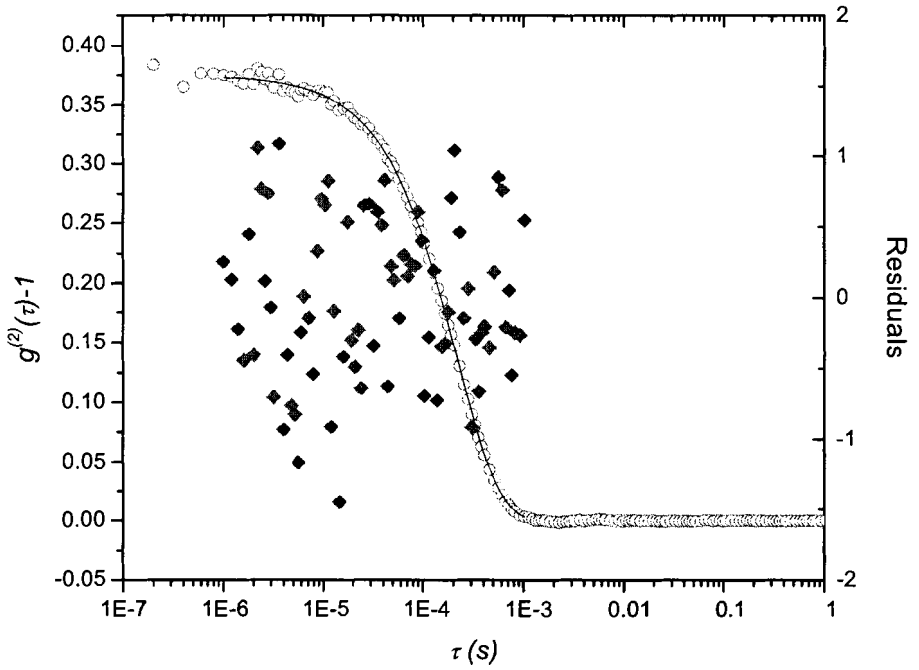

Figure 4.10: The autocorrelation function of the light scattered intensity $g^{(2)}(\tau) - 1$ for $PS - 67$ measured at a scattering angle of 90^o. The circles show the experimental data, the line shows the fit results for $\mu_2 \neq 0$ and the diamonds show the residuals.

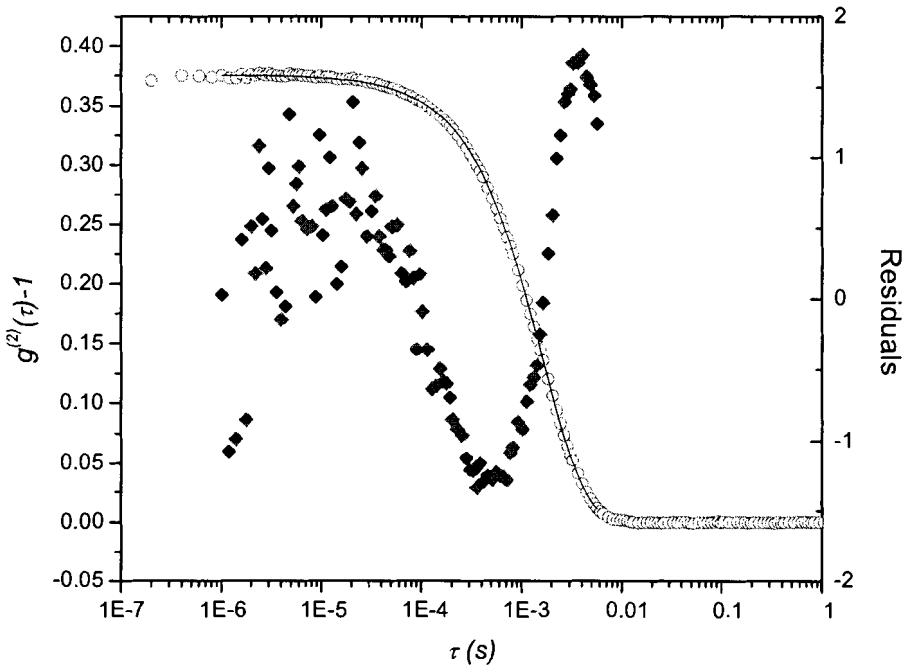

Figure 4.11: The autocorrelation function of the scattered light intensity $g^{(2)}(\tau) - 1$ for $PS - 67$ measured at a scattering angle of 30^o. The circles show the experimental data, the line shows the fit results for $\mu_2 = 0$ and the diamonds show the residuals.

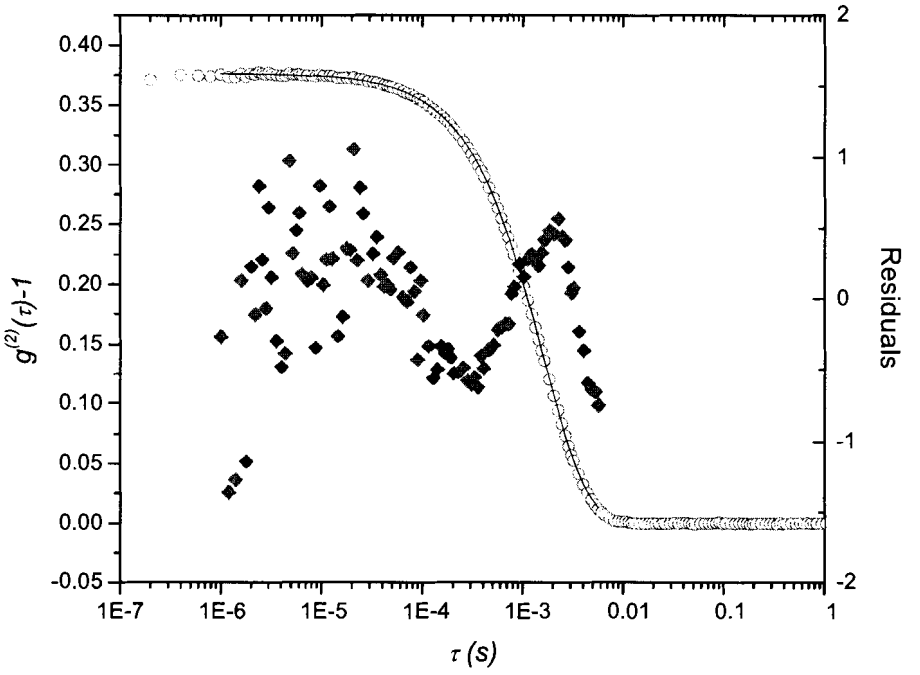

Figure 4.12: The autocorrelation function of the scattered light intensity $g^{(2)}(\tau) - 1$ for $PS - 67$ measured at a scattering angle of 30°. The circles show the experimental data, the line shows the fit results for $\mu_2 \neq 0$ and the diamonds show the residuals.

data sets at a scattering angle of 30^o.

	$\bar{\Gamma}_{first}$	μ_2	χ^2	$\bar{\Gamma}_{two}$	μ_2	χ^2
1	$617. \pm 1.$	0	0.72	$629. \pm 2.$	$(6. \pm 1.) \times 10^4$	0.36
2	$621. \pm 1.$	0	0.64	$635. \pm 2.$	$(7. \pm 1.) \times 10^4$	0.18
3	$619. \pm 1.$	0	0.81	$634. \pm 2.$	$(8. \pm 1.) \times 10^4$	0.28
4	$618. \pm 1.$	0	0.85	$634. \pm 2.$	$(8. \pm 1.) \times 10^4$	0.25
5	$620. \pm 1.$	0	0.65	$633. \pm 2.$	$(6. \pm 1.) \times 10^4$	0.27

Table 4.9: The fit results for $PS - 67$ at a scattering angle of 30^o.

The hydrodynamic radii inferred from the two types of fit are shown in Table 4.10 as a function of scattering angle.

	$R_h\,(nm)$	
Angle	$\mu_2 = 0$	μ_2 varied
30^o	37.27 ± 0.09	36.4 ± 0.1
40^o	37.27 ± 0.09	36.8 ± 0.2
50^o	37.2 ± 0.2	36.8 ± 0.2
60^o	37.3 ± 0.2	37.2 ± 0.3
70^o	37.5 ± 0.3	37.4 ± 0.1
80^o	37.5 ± 0.3	37.5 ± 0.4
90^o	37.4 ± 0.1	37.5 ± 0.3
100^o	37.6 ± 0.2	37.4 ± 0.1
110^o	37.7 ± 0.2	37.5 ± 0.4
120^o	37.9 ± 0.4	37.6 ± 0.4
130^o	37.8 ± 0.3	37.6 ± 0.6
140^o	38.0 ± 0.2	37.7 ± 0.4
150^o	38.1 ± 0.3	37.9 ± 0.2

Table 4.10: Hydrodynamic radii of $PS - 67$ at different scattering angles.

From the fit results for the polystyrene latex samples, we see that the values of μ_2 can have large differences even if the experimental data were measured under the same conditions. More importantly, the fit values of μ_2 are often negative; in contradiction with its definition. The hydrodynamic radii obtained for the two types of fits are consistent. In order to avoid the contradictions that the values of μ_2 are often negative, all the values of the hydrodynamic radii are obtained setting $\mu_2 = 0$. In order to avoid the problem that χ^2

is large, all fit results are chosen under this condition $\chi^2 < 2$. The results for the polystyrene latex samples measured at different scattering angles are shown in Appendix B.

4.2.2 Poly(N-isopropylacrylamide)(PNIPAM) Microgel Data and Results

Moment analysis was also used to obtain decay constants for PNIPAM samples using fits with $\mu_2 = 0$ and $\mu_2 \neq 0$ respectively. Figure 4.13 shows the results of fitting Eq. 2.50 to the $PNIPAM - 5$ data with $\mu_2 = 0$ over the delay time range 10^{-6} to 0.03927 s measured at a scattering angle of 30^o and a temperature of 29^oC. The residuals show systematic variations with the delay time. Figure 4.14 shows the same data along with a fit of Eq. 2.50 in which $\mu_2 \neq 0$. The residuals also show systematic variations with the delay time.

The fit results for both fits for the five independent data sets are listed in Table 4.11 for a scattering angle of 30^o and a temperature of 29^oC. The results for μ_2 are often negative, which is in contradiction with its definition. Since the residuals also show systematic variations with the delay time for the PS and PNIPAM microgel samples, why systematic variations can emerge needs to be further researched. Mostly the method of moment analysis needs to be reconsidered.

	$\bar{\Gamma}_{first}$	μ_2	χ^2	$\bar{\Gamma}_{two}$	μ_2	χ^2
1	90.4 ± 0.2	0	0.33	90.0 ± 0.3	$(-3. \pm 2.) \times 10$	0.32
2	90.9 ± 0.2	0	0.34	90.3 ± 0.3	$(-5. \pm 2.) \times 10$	0.29
3	90.2 ± 0.2	0	0.28	90.5 ± 0.3	$(2. \pm 2.) \times 10$	0.27
4	89.9 ± 0.2	0	0.25	89.8 ± 0.3	$-1. \pm 20$	0.25
5	90.4 ± 0.2	0	0.24	90.6 ± 0.3	$(2. \pm 2.) \times 10$	0.24

Table 4.11: The fit results for $PNIPAM - 5$ at a temperature of 29^oC and a scattering angle of 30^o.

With the fit results for the decay constant Γ and Eq. 2.51, the hydrodynamic radii R_h can be obtained. The values obtained for the two fits are shown in Table 4.12. Results are consistent for both fits.

The fit results for μ_2 show the same situation for the PNIPAM microgel samples as that obtained for the polystyrene latex samples: the values of μ_2 can have large differences even if the experimental data were measured under the same conditions, the fit values of μ_2 are often negative and the hydrodynamic radii obtained for the two types of fits are

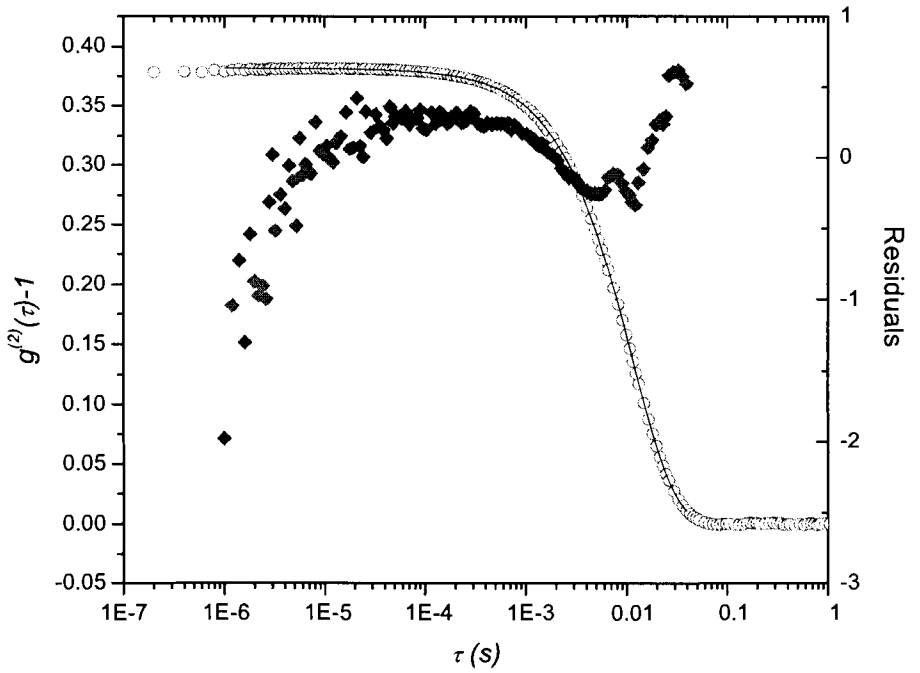

Figure 4.13: The autocorrelation function of the light scattered intensity $g^{(2)}(\tau) - 1$ for $PNIPAM - 5$ measured at a scattering angle of 30^o and a temperature of 29^oC. The circles show the experimental data, the line shows the fit results for $\mu_2 = 0$ and the diamonds show the residuals.

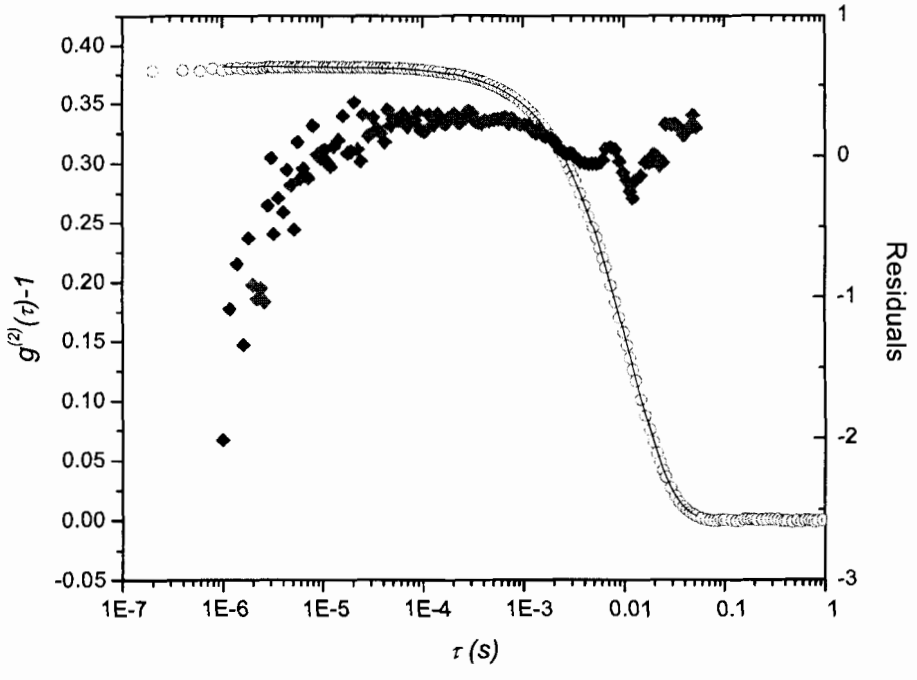

Figure 4.14: The auto-correlation function of the light scattered intensity $g^{(2)}(\tau) - 1$ for $PNIPAM - 5$ measured at a scattering angle of 30^o and a temperature of 29^oC. The circles show the experimental data, the line shows the fit results for $\mu_2 \neq 0$ and the diamonds show the residuals.

	$R_h\,(nm)$	
Angle	μ_2=0	μ_2 varied
30^o	$282. \pm 1.$	$283. \pm 1.$
35^o	$282. \pm 2.$	$283. \pm 1.$
40^o	$282. \pm 2.$	$282. \pm 2.$
45^o	$281. \pm 1.$	$283. \pm 2.$
50^o	$281. \pm 1.$	$281. \pm 1.$
55^o	$281. \pm 2.$	282.3 ± 0.8
60^o	$281. \pm 1.$	$281. \pm 1.$
65^o	$282. \pm 1.$	$282. \pm 1.$
70^o	280.3 ± 0.8	$281. \pm 1.$
75^o	$280. \pm 2.$	$281. \pm 2.$
80^o	$281. \pm 1.$	278.7 ± 0.7

Table 4.12: Hydrodynamic radii of $PNIPAM - 5$ at a temperature of 29°C and different scattering angles.

consistent. Only fits with $\mu_2 = 0$ will be considered, and all the values of the hydrodynamic radii are calculated in this situation later. Since the volumes of PNIPAM microgels display temperature sensitivity, the temperature is chosen as a parameter. All the results of apparent hydrodynamic radius are listed in Appendix B.

Chapter 5

Discussion

R_s and R_h reflect different physical characteristics of the particles. In this Chapter, the sizes of particles obtained using the different techniques will be discussed.

5.1 Polystyrene Latex Spheres

Sizes can be obtained using the DLS and SLS techniques respectively. The values are listed together in Table 5.1. As shown in Appendix B, the apparent hydrodynamic radius is a function of the scattering angle. Since the sizes of the three polystyrene samples are small, the values of R_h are almost independent of scattering angle. In order to compare the values obtained using different techniques, DLS results at the scattering angle of 40^o were chosen for all the PS samples.

$R_{TEM}\,(nm)$	$\langle R_s \rangle\,(nm)$	$R_h\,(nm)$	$R_h/\langle R_s \rangle$
33.5	33.3 ± 0.2	37.27 ± 0.09	1.119 ± 0.007
55	56.77 ± 0.04	64.5 ± 0.6	1.14 ± 0.01
90	92.05 ± 0.04	103.1 ± 0.4	1.120 ± 0.004

Table 5.1: The $\langle R_s \rangle$, commercial R_{TEM}, hydrodynamic radii R_h at a scattering angle of 40^o and the ratios $R_h/\langle R_s \rangle$ for PS samples.

From the results shown in Table 5.1, the size obtained using SLS is consistent with the commercial value R_{TEM} obtained using TEM. The value of the hydrodynamic radius obtained under the same conditions as the static radius is larger than that of the static

radius by about 12%.

The value of the root mean square radius of gyration $\langle R_g^2 \rangle_{cal}^{1/2}$ calculated using the commercial size distribution is consistent with the measured value of $\langle R_g^2 \rangle_{Zimm}^{1/2}$ obtained from the Zimm plot analysis. Also shown are values of $(R_g)_{R_s}$, the radius of gyration calculated from the mean static radius using the monodisperse model. The three values for each sample are consistent. This is because the distributions of the three PS samples are narrow. All results are shown in Table 5.2.

Sample	$\langle R_g^2 \rangle_{cal}^{1/2}$ (nm)	$\langle R_g^2 \rangle_{Zimm}^{1/2}$ (nm)	$(R_g)_{R_s}$ (nm)
$PS-67$	26.9	26.9 ± 0.5	25.8 ± 0.2
$PS-110$	43.2	46.8 ± 0.3	44.00 ± 0.03
$PS-180$	70.1	$69. \pm 2.$	71.34 ± 0.03

Table 5.2: Values of $\langle R_g^2 \rangle_{cal}^{1/2}$, $\langle R_g^2 \rangle_{Zimm}^{1/2}$ and $(R_g)_{R_s}$ (nm).

Next, the dimensionless parameters ρ and $\langle R_g^2 \rangle_{Zimm}^{1/2} / \langle R_s \rangle$ will be discussed. The values of the dimensionless parameters ρ and $\langle R_g^2 \rangle_{Zimm}^{1/2} / \langle R_s \rangle$ and the ratios σ/R_{TEM} for the PS samples are shown in Table 5.3.

Sample	ρ	$\langle R_g^2 \rangle_{Zimm}^{1/2} / \langle R_s \rangle$	σ/R_{TEM}
$PS-67$	0.72 ± 0.01	0.81 ± 0.02	0.075
$PS-110$	0.726 ± 0.008	0.824 ± 0.005	0.045
$PS-180$	0.67 ± 0.02	0.75 ± 0.02	0.028

Table 5.3: The dimensionless parameters of ρ and $\langle R_g^2 \rangle_{Zimm}^{1/2} / \langle R_s \rangle$ and the ratios σ/R_{TEM} for the PS samples.

The value of $\langle R_g^2 \rangle_{Zimm}^{1/2}$ is influenced by the standard deviation of particle sizes. This is shown in Table 5.4 where values of $\langle R_g^2 \rangle_{cal}^{1/2} / \langle R \rangle$ are shown calculated for particle size distributions with different relative widths $\sigma / \langle R \rangle$.

As seen in Table 5.4, the values of the dimensionless shape parameter of polydisperse systems should be larger than the value 0.775, which is the theoretical value for monodisperse homogenous particle systems. Values for ρ are certainly less than expected. However the values for $\langle R_g^2 \rangle_{Zimm}^{1/2} / \langle R_s \rangle$ are generally consistent. For the samples $PS-67$ and $PS-110$,

$\sigma / \langle R \rangle$	$\langle R_g^2 \rangle_{cal}^{1/2} / \langle R \rangle$
0	0.775
0.04	0.783
0.07	0.799
0.1	0.822

Table 5.4: The values of $\langle R_g^2 \rangle_{cal}^{1/2} / \langle R \rangle$ with different distribution widths.

very good linear ranges of $\frac{Kc}{R_{vv}}$ as a function q^2 can be obtained and values of $\langle R_g^2 \rangle_{Zimm}^{1/2}$ can be measured accurately. For the sample $PS - 180$, the value of $\langle R_g^2 \rangle_{Zimm}^{1/2}$ is affected by the fit range. The value changes from 66 nm to 72 nm as the different fit data points were chosen. It is thus difficult to determine the value of $\langle R_g^2 \rangle_{Zimm}^{1/2}$. This situation arises because a good linear range of $\frac{Kc}{R_{vv}}$ as a function q^2 cannot be obtained. Even if the data can be measured at much smaller angles, there still exist other problems; at small angles, the experimental data stringently depend on sample quality and instrument capability. These problems constraint the use of Zimm plot analysis to small particles.

5.2 Poly(N-isopropylacrylamide)($PNIPAM$) Microgel

5.2.1 Temperature Dependence of the Sizes for the Four PNIPAM Microgel Samples

When the temperature is increased from 25^oC to 40^oC, the characteristics of PNIPAM microgel particles change from being hydrophilic to hydrophobic. The volumes of PNIPAM particles collapse. The change of the size of the PNIPAM microgels with temperature can be observed using light scattering techniques. Figures 5.1-5.4 compare the temperature dependence of R_h and $\langle R_s \rangle$ for $PNIPAM-5$, $PNIPAM-2$, $PNIPAM-1$ and $PNIPAM-0$, respectively. Since the uncertainties of the mean static and hydrodynamic radii are very small as shown in Appendix A and B, the values of the mean static radii and hydrodynamic radii only were shown. These figures show that the mean static radii of the four PNIPAM microgel samples is generally decreasing as the temperatures is increased. Near the transition temperature, the radii decrease sharply.

Even far from the transition, the large negative thermal expansion coefficient $\chi_V = \frac{\partial V}{V \partial T}$

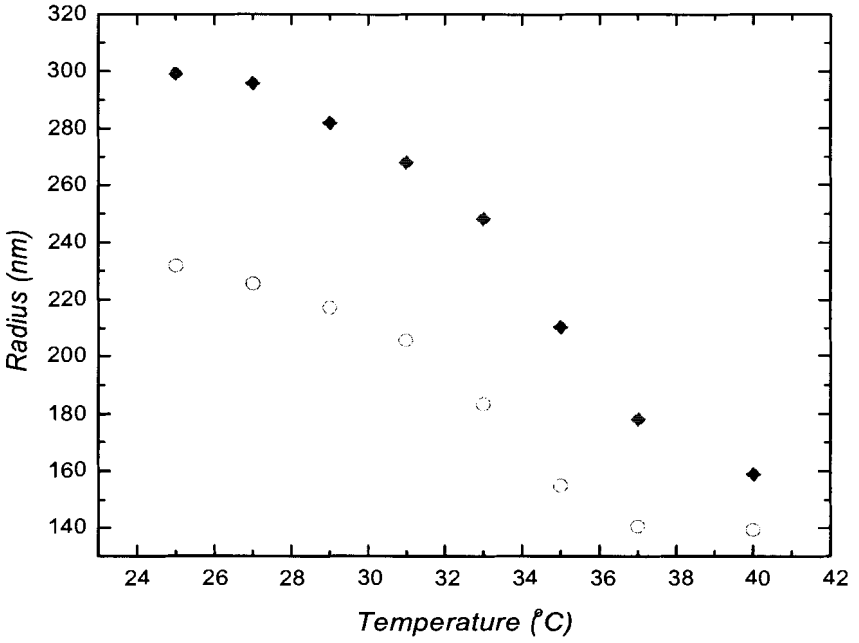

Figure 5.1: The hydrodynamic radii (*diamonds*) measured at a scattering angle of 30^o and the static radii (*circles*) of $PNIPAM - 5$ at different temperatures.

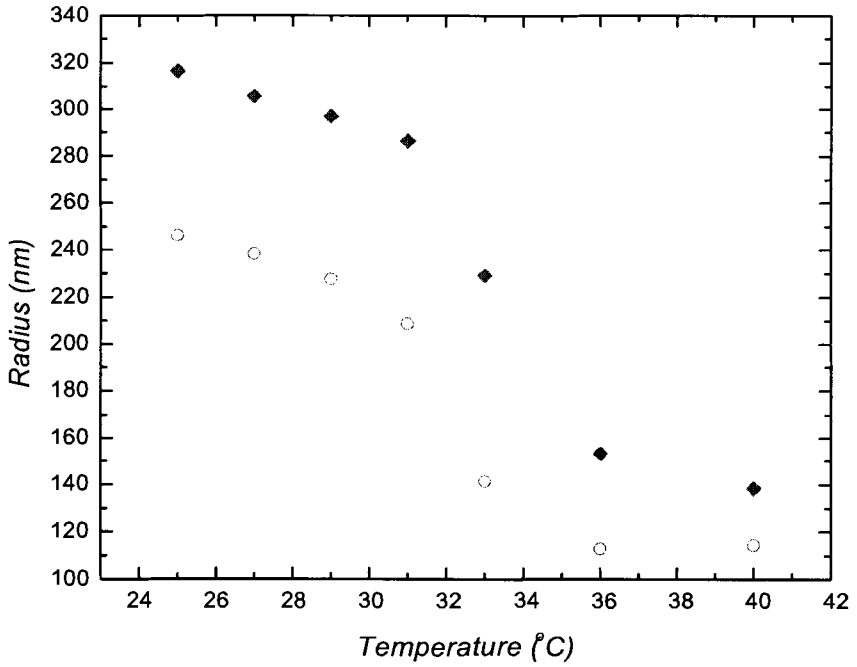

Figure 5.2: The hydrodynamic radii (*diamonds*) measured at a scattering angle of 30^o and the static radii (*circles*) of $PNIPAM-2$ at different temperatures.

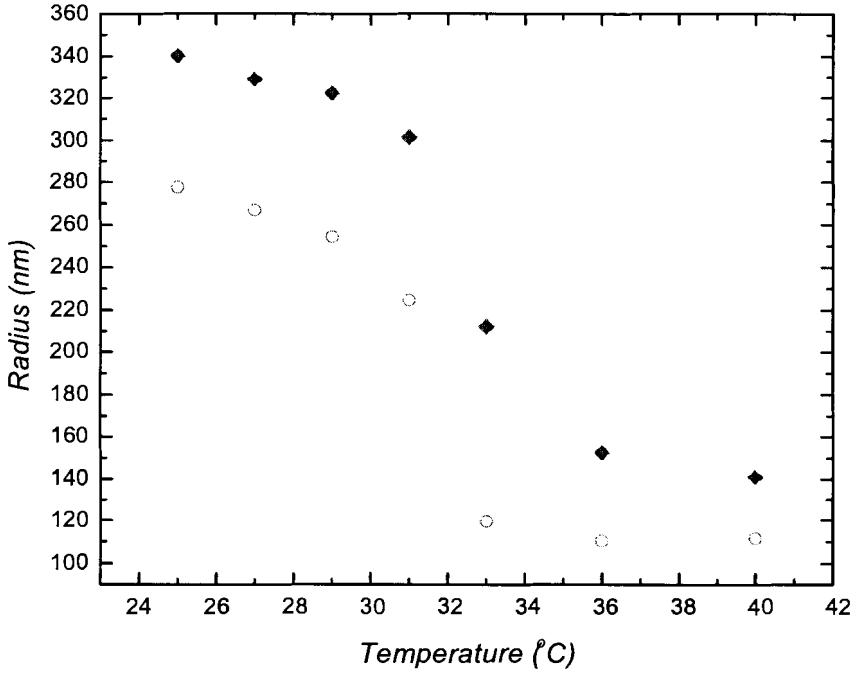

Figure 5.3: The hydrodynamic radii (*diamonds*) measured at a scattering angle of 30^o and the static radii (*circles*) of $PNIPAM-1$ at different temperatures.

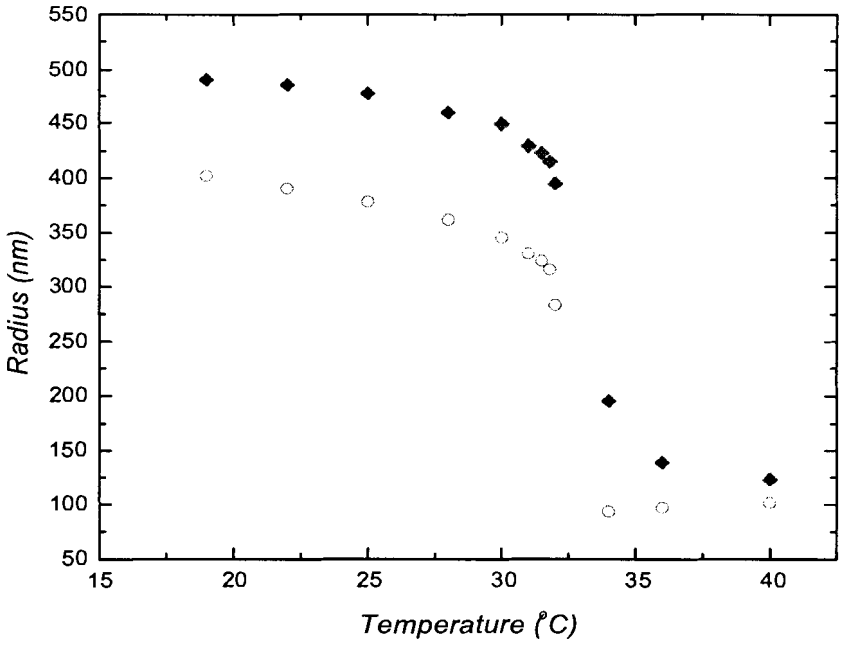

Figure 5.4: The hydrodynamic radii (*diamonds*) measured at a scattering angle of 30^o and the static radii (*circles*) of $PNIPAM - 0$ at different temperatures.

is surprising. Some results for χ_V calculated from $\langle R_s \rangle$ are listed in Table 5.5, 5.6 and 5.7 for $PNIPAM-5$, $PNIPAM-2$, $PNIPAM-1$ and $PNIPAM-0$, respectively.

Temperature range (^oC)	$\chi_V = \frac{\Delta V}{V \Delta T}$ $(^oC^{-1})$
25-27	-0.041
27-29	-0.059
29-31	-0.076
31-33	-0.16
33-35	-0.23
35-37	-0.14
37-40	-0.0092

Table 5.5: The approximate values of the thermal expansion coefficient for $PNIPAM-5$.

Temperature range (^oC)	$\chi_V = \frac{\Delta V}{V \Delta T}$ $(^oC^{-1})$	
	$PNIPAM-2$	$PNIPAM-1$
25-27	-0.048	-0.058
27-29	-0.068	-0.071
29-31	-0.13	-0.17
31-33	-0.48	-0.70
33-36	-0.20	-0.077
36-40	0.010	0.0086

Table 5.6: The approximate values of the thermal expansion coefficient for $PNIPAM-2$ and $PNIPAM-1$.

Even at temperatures far away the transition, χ_V still is about -10^{-2} $(^oC^{-1})$ below and above the phase transition. However the thermal linear expansion coefficients, $\alpha = (\partial L/\partial T)_P / L$, of polymers (vulcanized rubber) [35] are about -10^{-4} $(^oC^{-1})$, where P and L represent the pressure and the length of samples, respectively. For small deformations of particles, there exists a relationship $\chi_V = 3\alpha$. From this relationship, our values show a large difference with results expected for polymers. In order to understand this difference, the structures of PNIPAM microgel particles need to be considered. PNIPAM microgel particles comprise two components: one is the polymer and the other is the water molecules. When temperature changes, the PNIPAM microgel particles can absorb or release the water molecules, so this system can be considered to be an open system. For an open system, the

Temperature range (°C)	$\chi_V = \frac{\Delta V}{V \Delta T}$ $(^oC^{-1})$
19-22	-0.031
22-25	-0.031
25-28	-0.043
28-30	-0.066
30-31	-0.128
31-31.5	-0.125
31.5-31.8	-0.256
31.8-32	-1.53
32-34	-1.01
34-36	0.066
36-40	0.036

Table 5.7: The approximate values of the thermal expansion coefficient for $PNIPAM - 0$.

thermal expansion coefficient χ_V is defined as $\chi_V = \frac{1}{V}\left(\frac{\partial V}{\partial T}\right)_{P,N_i}$. Since water molecules can flow out or into the PNIPAM microgel particles as the temperature changes, these results of the thermal expansion coefficient may represent the change of water molecules inside the PNIPAM microgel particles.

At the transition, the radius changes more quickly with temperature. In order to understand this behavior of PNIPAM microgel particles, the peculiarities of water as a liquid must be considered. In general it is agreed that water is a highly hydrogen-bonded liquid [39]. When solutes and solute groupings are added to water, they disrupt the local structure of the water and new structure is formed in the region of the added solutes. Hydrophilic nonionic solutes form hydrogen bonds with the water molecules. The water-water contacts are replaced by polymer-water contacts. Regular structure can be formed and can compensate for the water-water bonds broken. Meanwhile the hydrophobic parts of the solutes interact with water via the hydrophobic effect: because of the existence of nonpolar regions of the solutes, the water molecules must reorient around them.

A closer look at the structure of PNIPAM, as shown in Fig. 5.5, will help us to understand the peculiar volume phase transition properties of PNIPAM in water [34]. The oxygen and nitrogen atoms have a net negative charge and the hydrogen interacting with the nitrogen brings some net positive charge due to the perturbation of the electrons. This region of the molecule can then form hydrogen bonds with the surrounding water molecules. Other parts of the PNIPAM are hydrophobic. The characteristics of PNIPAM in water are

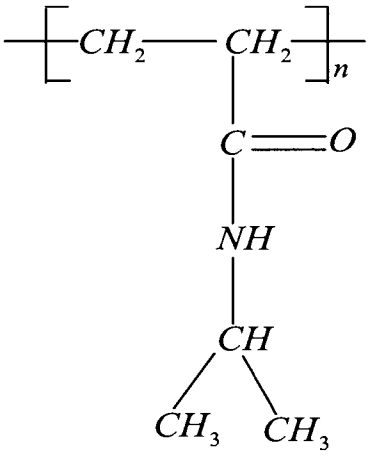

Figure 5.5: The chemical structure of Poly(N-isopropylacrylamide).

mainly determined by the relationship between the hydrophilic and hydrophobic effects. At low temperatures, hydrogen bonds forming between the water molecules and the PNIPAM molecules are more efficient than hydrogen bonds forming between water molecules only. This makes the PNIPAM to dissolve in water. As a result, PNIPAM microgel particles swell. As the temperature increases, the polymer-water contacts become weak and are replaced by water-water and polymer-polymer contacts [34]. The PNIPAM molecules collapse suddenly as the temperature is raised. This is called volume phase transition (VPT). Above the VPT, the interaction between PNIPAM and water becomes hydrophobic.

5.2.2 Relation between R_h and $\langle R_s \rangle$

The sizes obtained from DLS and SLS for both the PS and PNIPAM microgel samples show that the apparent hydrodynamic radius R_h is larger than the static radius $\langle R_s \rangle$. From the definition, the radii R_h and $\langle R_s \rangle$ represent the sizes of particles obtained from the different physical characteristics of the samples. The apparent hydrodynamic radius R_h is mainly determined by the hydrodynamic features of particles.

The discrepancy between R_h and R_s could be due to use of the Stokes-Einstein relation to calculate R_h from the diffusion coefficient. The Stokes-Einstein relation is obtained when

the movements of particles are diffusion processes for no slip boundary conditions. As the particle translates through a fluid of viscosity η_0 with velocity v, the drag force F_{drag} on a particle is written as

$$F_{drag} = 6\pi\eta_0 R_h v. \tag{5.1}$$

For real samples, there may exist some deviations from the conditions under which the Stokes-Einstein relation can be used. For example, there may be polymer chains dangling from the surface and the surfaces may be coarse. These deviations would make the drag force on a particle appear to be larger. If the hydrodynamic radius is still obtained using the Stokes-Einstein relation, the values obtained will be too large. This is why ρ is still less than 0.775 for the PS and PNIPAM samples, although the values of $\langle R_g^2 \rangle_{Zimm}^{1/2}$ become bigger.

5.2.3 Crosslinker Dependence

In all cases, the sizes of the PNIPAM microgel particles decrease with temperature. In order to show the effects of adding crosslinker on the volume phase transition, the size of this decrease observed for different crosslinker contents as obtained from SLS and DLS measurements are shown in Figs. 5.6 and 5.7, respectively. The radius is compared to that measured at a temperature of 40°C. A few authors [[17],[18]] have shown similar results for R_h; in their papers, the phase transition was shown with the PNIPAM microgel samples where the crosslinker content varies over a much wider range.

There are two possible reasons why the phase transition becomes less sharp and weaker as crosslinker is incorporated. One is that the added crosslinker increases the number of physical crosslinking points. The more crosslinking points, the larger the elasticity of the gel particles. The PNIPAM microgel particles thus cannot be deformed as easily. The other is that more crosslinking points result in a stronger hydrophobic interaction due to the hydrophobic features of the crosslinker [36]. The total experimental result of adding crosslinker is that the phase transition of PNIPAM becomes less sharp and the change in radius becomes smaller as the cross-linker content increases. The theoretical explanation can be studied further.

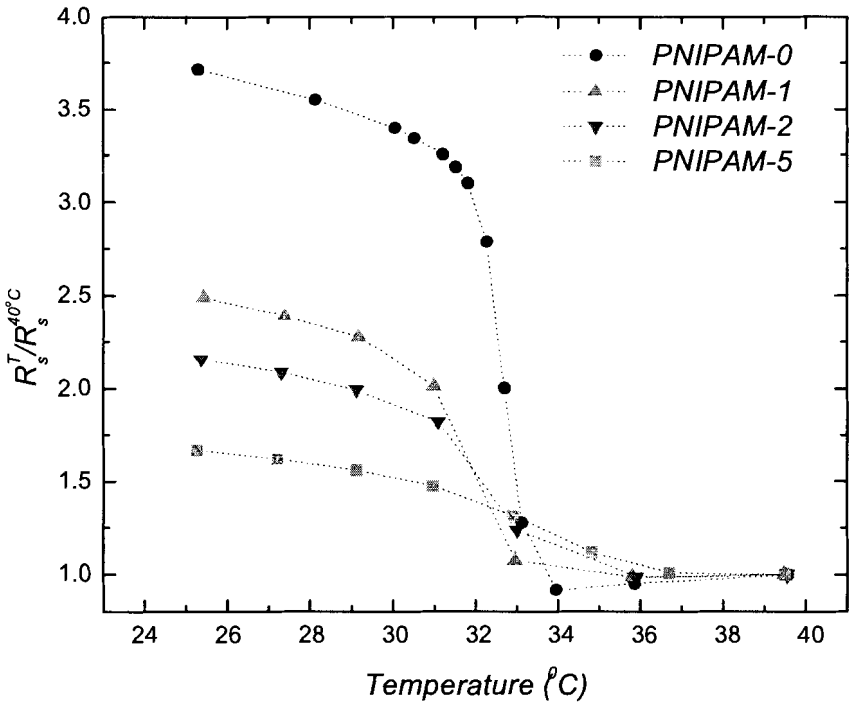

Figure 5.6: The ratios of the static radii at temperature T $\left(R_s^T\right)$ to that measured at 40°C $\left(R_s^{40^oC}\right)$ for $PNIPAM-0$, $PNIPAM-1$, $PNIPAM-2$ and $PNIPAM-5$.

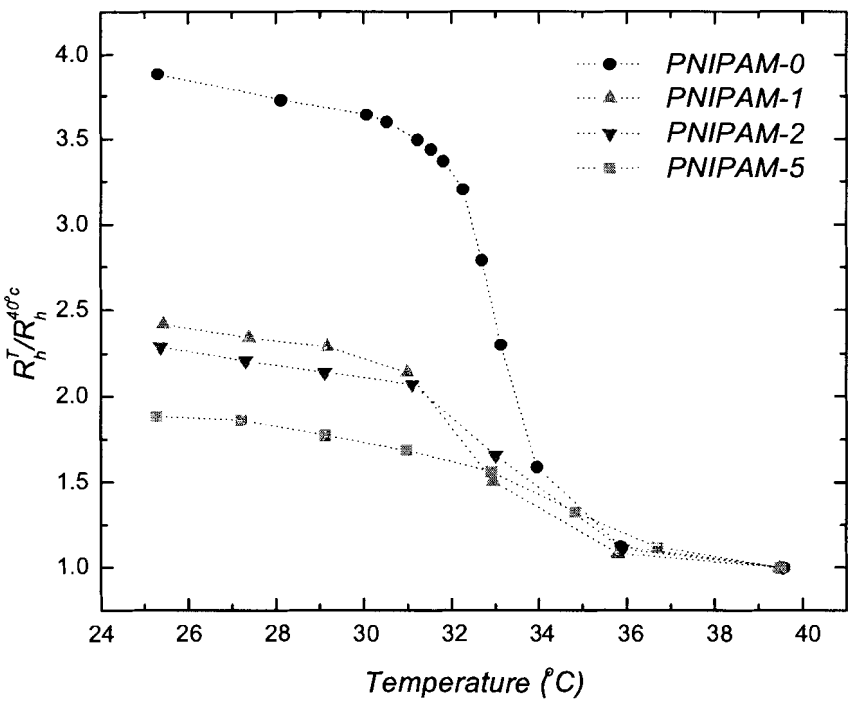

Figure 5.7: The ratios of the hydrodynamic radii at temperature T $\left(R_h^T\right)$ to that measured at 40°C $\left(R_h^{40°C}\right)$ for $PNIPAM-0$, $PNIPAM-1$, $PNIPAM-2$ and $PNIPAM-5$ at the scattering angle 30^o.

5.2.4 Ratio of the Apparent Hydrodynamic Radius over the Mean Static Radius near VPT

The static radius reflects the mass distribution and the apparent hydrodynamic radius reflects both the mass distribution and the hydrodynamic features of the PNIPAM microgel particles. As the temperature changes, it is possible that the mass distribution and hydrodynamic features of the PNIPAM microgel particles are influenced differently. In order to show this feature, the temperature dependence of the ratio $R_h^T / \langle R_s^T \rangle$ is shown in Fig. 5.8 for the four PNIPAM microgels samples.

As shown in Fig 5.8, the ratio of the apparent hydrodynamic radius over the mean static radius is larger than 1 in the temperature range from 24^oC to 40^oC. Below and above the phase transition, the values of the ratio change from 1.1 to 1.3. When the temperature nears the phase transition temperature, the values of the ratios become larger and the peaks emerge. The lower the crosslinker content, the higher the peak in the ratio $R_h^T / \langle R_s^T \rangle$. The variation in the temperature dependence of the ratios $R_h^T / \langle R_s^T \rangle$ for the four PNIPAM microgel samples shows that the volume phase transition has different effects on the mass distribution and on the hydrodynamic characteristics of the particles. In order to obtain more information from the relationship between R_h and R_s, R_h needs to be further studied.

5.2.5 Shape Parameter

The fact that the static radius $\langle R_s \rangle$ is not equal to the hydrodynamic radius R_h under the same conditions raises an interesting question: Can the dimensionless shape parameter ρ tell us anything about the particle shape? From Eq. 2.30, the definition of the root mean square radius of gyration $\langle R_g^2 \rangle_{Zimm}^{1/2}$ is a function of the mean static radius $\langle R_s \rangle$ and distribution for spherical particles. For the monodisperse model, R_g is only related to R_s and has a value of $R_g/R_s = 0.775$ for homogenous spherical particles. At present, the definition of the dimensionless shape parameter is $\langle R_g^2 \rangle_{Zimm}^{1/2} / \langle R_h \rangle$. All the theoretical values of ρ have been derived for the different shape particles with a monodisperse distribution. For homogenous spherical particles, the value of ρ is, by definition, 0.775. For the four PNIPAM microgel samples, the values of parameters $\langle R_g^2 \rangle_{Zimm}^{1/2} / \langle R_s \rangle$ and ρ calculated using the values of the hydrodynamic radius at a scattering angle of 30^oC are listed in Table 5.8. The expected values of $\langle R_g^2 \rangle_{cal}^{1/2} / \langle R_s \rangle$ obtained using the mean static radius and standard deviation and Eq. 2.30 also are shown in Table 5.8.

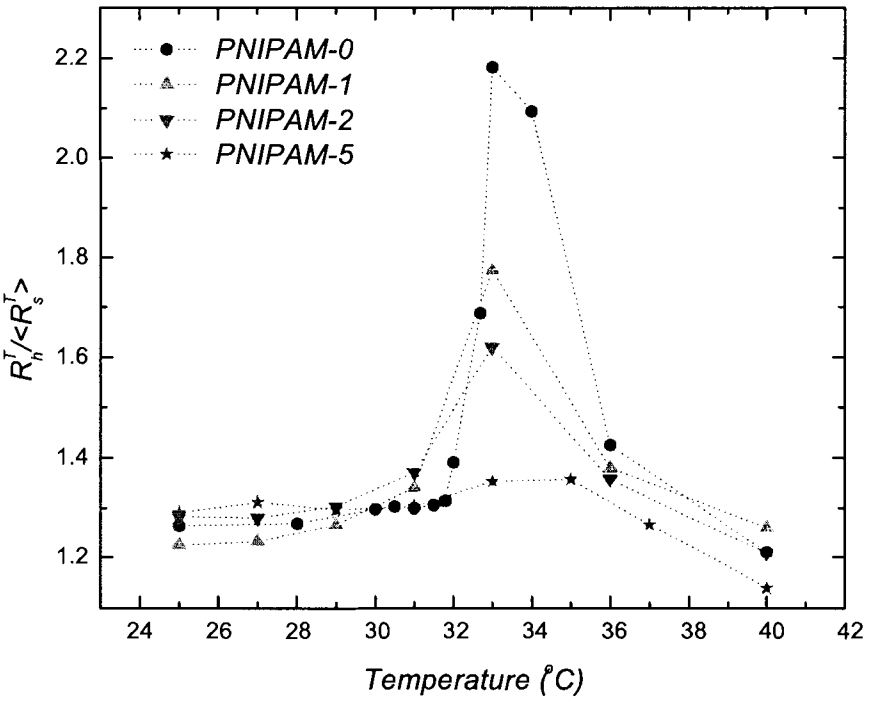

Figure 5.8: The ratios between the hydrodynamic and static radii $R_h^T / \langle R_s^T \rangle$ for $PNIPAM-0$, $PNIPAM-1$, $PNIPAM-2$ and $PNIPAM-5$ measured under the same conditions.

Sample (Temperature)	ρ	$\langle R_g^2 \rangle_{Zimm}^{1/2} / \langle R_s \rangle$	$\langle R_g^2 \rangle_{cal}^{1/2} / \langle R_s \rangle$
$PNIPAM-5\ (40^oC)$	0.73 ± 0.02	0.83 ± 0.03	0.813 ± 0.003
$PNIPAM-2\ (40^oC)$	0.69 ± 0.03	0.84 ± 0.04	0.82 ± 0.01
$PNIPAM-1\ (40^oC)$	0.69 ± 0.03	0.87 ± 0.04	0.856 ± 0.009
$PNIPAM-0\ (40^oC)$	0.66 ± 0.01	0.80 ± 0.02	0.81 ± 0.01
$PNIPAM-0\ (34^oC)$	0.54 ± 0.02	1.13 ± 0.03	1.04 ± 0.03

Table 5.8: The values of the dimensionless parameters of ρ, $\langle R_g^2 \rangle_{Zimm}^{1/2} / \langle R_s \rangle$ and $\langle R_g^2 \rangle_{cal}^{1/2} / \langle R_s \rangle$.

From Table 5.8, the calculated value $\langle R_g^2 \rangle_{cal}^{1/2} / \langle R_s \rangle$ is consistent with the experimental value $\langle R_g^2 \rangle_{Zimm}^{1/2} / \langle R_s \rangle$ and the value of ρ has large differences with the experimental value $\langle R_g^2 \rangle_{Zimm}^{1/2} / \langle R_s \rangle$. Meanwhile from Eq. 2.28 or 2.30, the values of $\langle R_g^2 \rangle_{Zimm}^{1/2} / \langle R_s \rangle$ are larger than 0.775. For a wide distribution, $\langle R_g^2 \rangle_{Zimm}^{1/2} / \langle R_s \rangle$ can even be larger than 1. Just like the sample $PNIPAM-0$ at a temperature of 34°C, the expected value of $\langle R_g^2 \rangle_{cal}^{1/2} / \langle R_s \rangle$ is 1.04 and the value of ρ is only 0.538. Compared with the experimental value 1.13, ρ cannot give a good description for the shape of particles. The dimensionless parameter $\langle R_g^2 \rangle^{1/2} / \langle R_s \rangle$ not only gives a good description of the particle shape, but also reflects the effects of the distribution of particle sizes.

Chapter 6

Conclusion

The relationship between the scattered intensity per unit volume and the scattering vector described in Chapter 2 (Eq. 2.28) provides one method to measure accurately the particle size distribution. With it, narrow particle size distributions that cannot be measured using moments analysis have been obtained.

Comparing results of SLS and DLS shows that more accurate information about the size distribution can be obtained from SLS data. The results obtained from SLS avoid the problems encountered in the analyzing DLS data that the apparent hydrodynamic radius depends on scattering angle. Meanwhile, as shown in Table 5.1, the SLS results agree with values as measured using TEM. Another important aspect is that the distribution obtained from the SLS data is the number size distribution $G(R_s)$. Compared to the distribution $G(R_h)$, which is a composite distribution, $G(R_s)$ gives direct information about the particle size distribution. Since the more accurate size distribution obtained from SLS data can affect the analysis of all physical quantities that are related to the particle size distribution, the influences can be further explored.

Based on our results, the size measured using the SLS technique is not equal to that measured using DLS technique even for polystyrene latex sphere samples. For PS samples, this difference is about 12%. For the PNIPAM microgel samples, the difference is much larger and ranges from about 20% both below and above the transition to about 110% at the transition. For PNIPAM the largest deviations were observed for the lowest crosslinker concentrations. The results show that the structure of PNIPAM microgel particles are related to the amount of the crosslinker. Since many features of structure can influence the values of the apparent hydrodynamic radius of PNIPAM microgel particles, for example:

the dangling chains, the coarse surfaces and the hydrogen bonds, etc, how the contents of crosslinker affects the structures of PNIPAM microgel particles can be further studied.

The expected value of $\langle R_g^2 \rangle_{cal}^{1/2}$ calculated using the commercial mean radius and standard deviation is the same as the measured result using the Zimm plot analysis. This consistency also shows that the measured values obtained using the SLS technique are more accurate. In general, the value of $\langle R_g^2 \rangle_{Zimm}^{1/2}$ is a function of the particle size distribution of the particles and the ratio of $\langle R_g^2 \rangle_{Zimm}^{1/2} / \langle R_s \rangle$ is larger than 0.775. The dimensionless shape parameter ρ cannot provide a good description for the shapes of particles in the presence of polydispersity and when the results for R_h are inaccurate.

Appendix A

Details of results obtained using SLS

Temperature(°C)	$\langle R_s \rangle (nm)$	$\sigma (nm)$	$\sigma / \langle R_s \rangle$	χ^2
25	231.9 ± 0.7	20.7 ± 1.0	0.089	1.49
27	225.6 ± 0.4	17.4 ± 0.7	0.077	2.44
29	216.7 ± 0.3	18.3 ± 0.5	0.084	1.07
31	205.7 ± 0.2	15.2 ± 0.5	0.074	1.22
33	183.6 ± 0.5	14.4 ± 0.9	0.078	5.36
35	155.2 ± 0.1	10.75 ± 0.01	0.069	6.32
37	140.6 ± 0.3	16.2 ± 0.6	0.115	11.30
40	139.3 ± 0.3	12.4 ± 0.6	0.089	5.50

Table A.1: The fit results for $PNIPAM - 5$ at different temperatures.

Temperature(^{o}C)	$\langle R_s \rangle (nm)$	$\sigma (nm)$	$\sigma / \langle R_s \rangle$	χ^2
25	246.5 ± 0.2	22.6 ± 0.4	0.092	4.70
27	238.6 ± 0.9	18.5 ± 0.3	0.078	1.63
29	227.8 ± 0.2	19.9 ± 0.4	0.087	1.03
31	208.8 ± 0.3	18.8 ± 0.5	0.090	2.65
33	141.3 ± 0.6	14.8 ± 0.8	0.105	5.65
36	112.9 ± 1.2	14.9 ± 1.1	0.132	3.84
40	114.4 ± 0.9	11.4 ± 1.1	0.100	4.34

Table A.2: The fit results for $PNIPAM - 2$ at different temperatures.

Temperature(^{o}C)	$\langle R_s \rangle (nm)$	$\sigma (nm)$	$\sigma / \langle R_s \rangle$	χ^2
25	277.7 ± 0.5	23.1 ± 0.9	0.083	1.84
27	267.1 ± 0.5	23.1 ± 0.8	0.087	2.50
29	254.3 ± 0.1	21.5 ± 0.3	0.084	2.15
31	224.8 ± 0.9	30.6 ± 0.9	0.136	3.31
33	$120. \pm 1.$	20.1 ± 0.7	0.168	3.80
36	110.4 ± 0.9	17.3 ± 0.7	0.157	4.19
40	111.7 ± 0.9	14.8 ± 0.8	0.133	2.73

Table A.3: The fit results for $PNIPAM - 1$ at different temperatures.

Temperature(^{o}C)	$\langle R_s \rangle (nm)$	$\sigma (nm)$	$\sigma / \langle R_s \rangle$	χ^2
19	402.1 ± 0.3	36.7 ± 0.6	0.091	1.06
22	390.0 ± 0.4	36.3 ± 0.5	0.093	1.33
25	377.8 ± 0.4	37.0 ± 0.5	0.098	1.57
28	361.5 ± 0.3	36.6 ± 0.4	0.101	0.44
30	345.5 ± 0.4	37.2 ± 0.7	0.108	2.25
31	330.8 ± 0.4	38.3 ± 0.5	0.116	5.11
31.5	323.9 ± 0.4	39.1 ± 0.3	0.121	11.08
31.8	315.6 ± 0.3	39.3 ± 0.3	0.125	1.75
32	283.4 ± 0.5	42.6 ± 0.9	0.150	2.39
34	93.4 ± 1.9	24.5 ± 0.9	0.262	1.56
36	97.1 ± 3.0	14.1 ± 2.1	0.145	7.20
40	101.7 ± 1.1	8.6 ± 1.3	0.085	1.80

Table A.4: The fit results for $PNIPAM - 0$ at different temperatures.

Appendix B

Details of results obtained using DLS

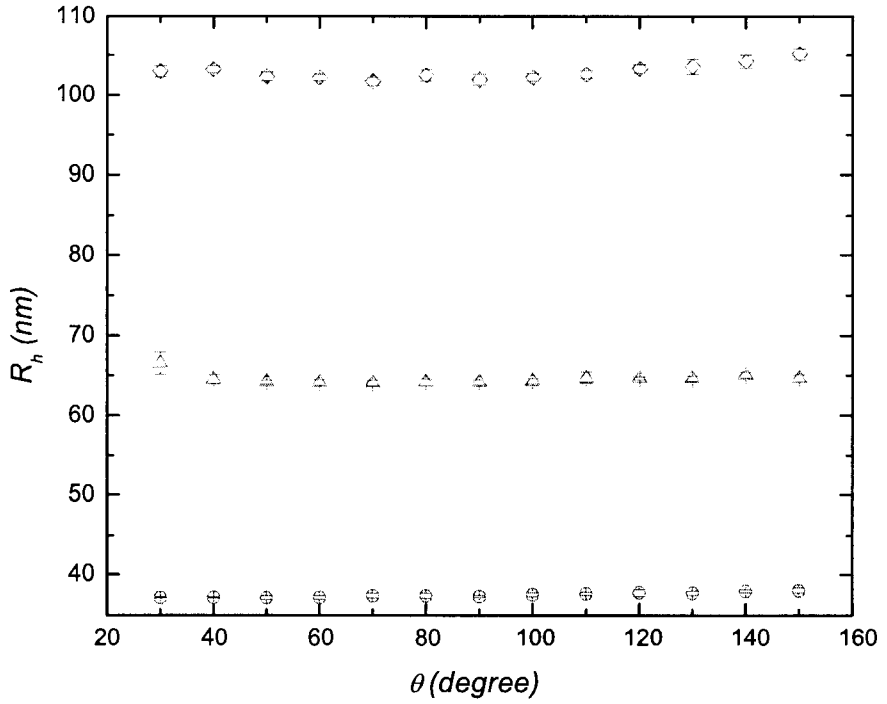

Figure B.1: Hydrodynamic radii as a function of scattering angle θ for polystyrene latex spheres. Circles, Triangles and Diamonds show the results for spheres with nominal mean radii 33.5 nm, 55 nm and 90 nm, respectively.

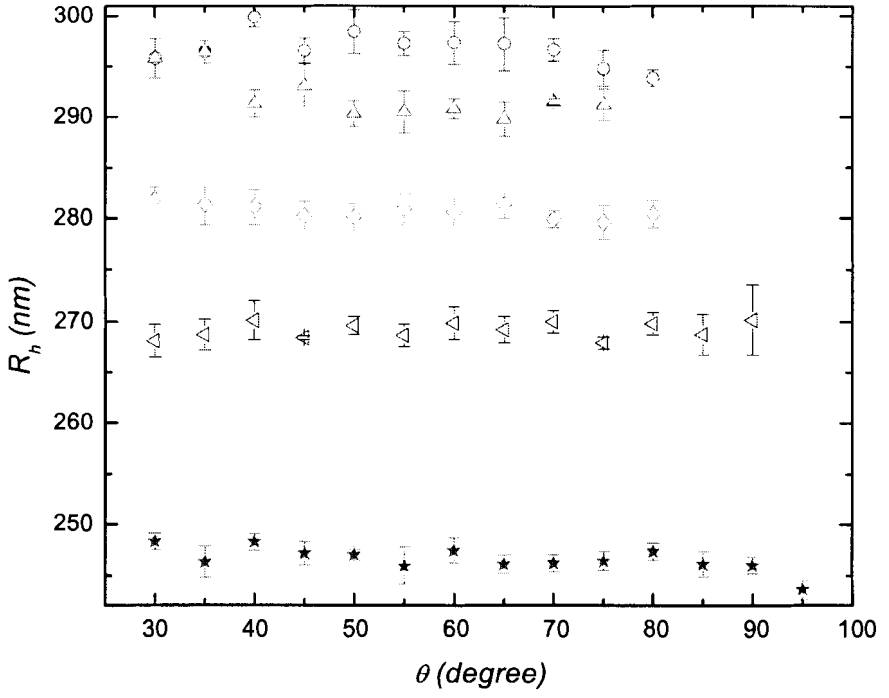

Figure B.2: Hydrodynamic radii as a function of scattering angle θ for $PNIPAM - 5$ at 25°C ($\circ$), 27°C ($\triangle$), 29°C ($\diamond$), 31°C ($\triangleleft$) and 33°C ($\star$).

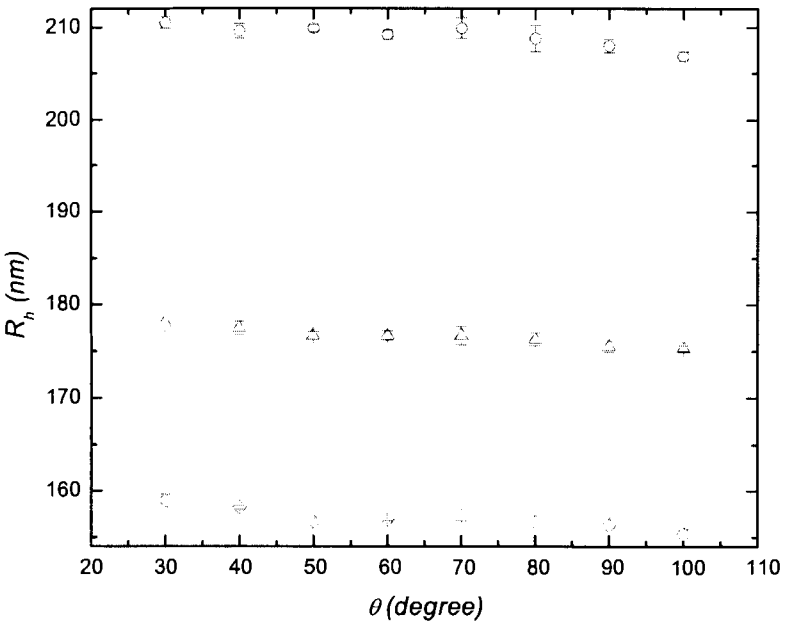

Figure B.3: Hydrodynamic radii as a function of scattering angle θ for $PNIPAM - 5$ at 35^oC ($\circ$), 37^oC ($\triangle$) and 40^oC ($\diamond$).

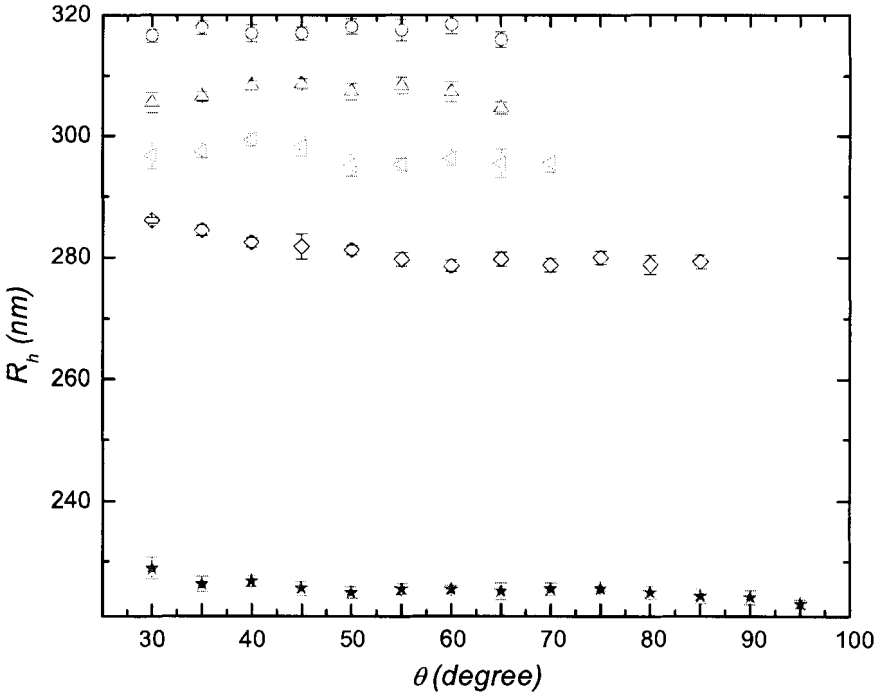

Figure B.4: Hydrodynamic radii as a function of scattering angle θ for $PNIPAM - 2$ at 25^oC ($\circ$), 27^oC ($\triangle$), 29^oC ($\diamond$), 31^oC ($\triangleleft$) and 33^oC ($\star$).

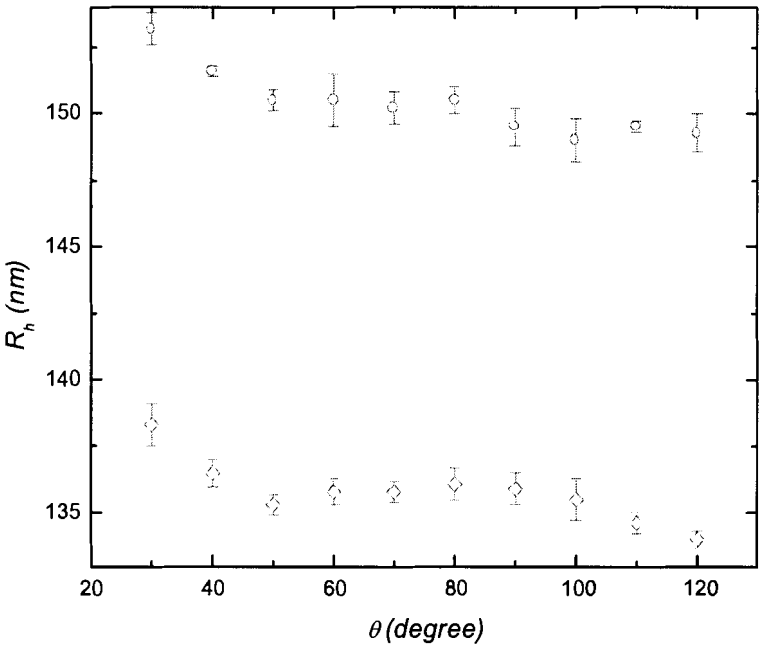

Figure B.5: Hydrodynamic radii as a function of scattering angle θ for $PNIPAM - 2$ at 36°C (○) and 40°C (◇).

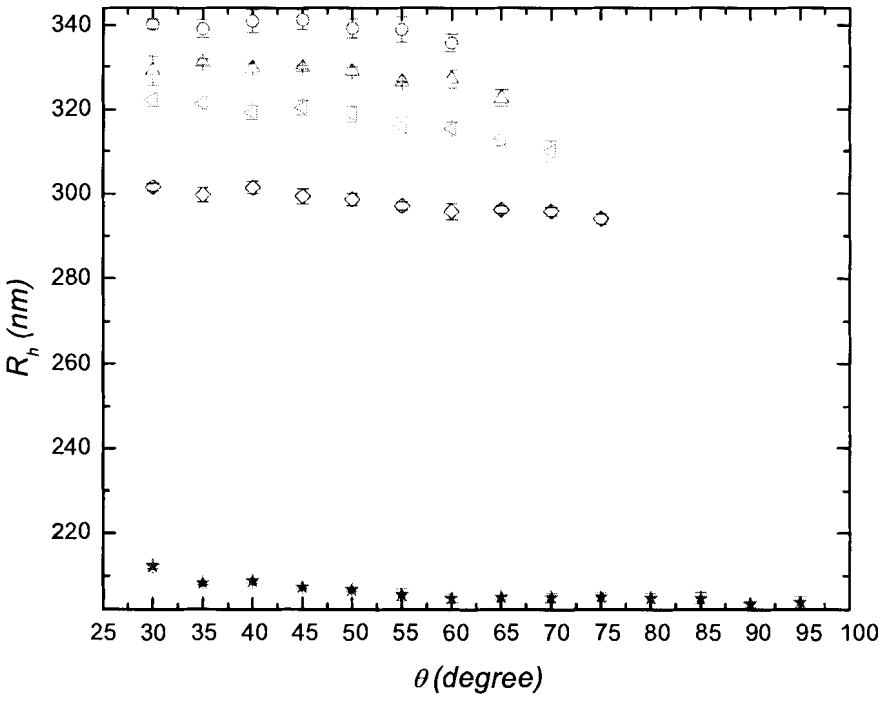

Figure B.6: Hydrodynamic radii as a function of scattering angle θ for $PNIPAM - 1$ at 25°C ($\circ$), 27°C ($\triangle$), 29°C ($\diamond$), 31°C ($\triangleleft$) and 33°C ($\star$).

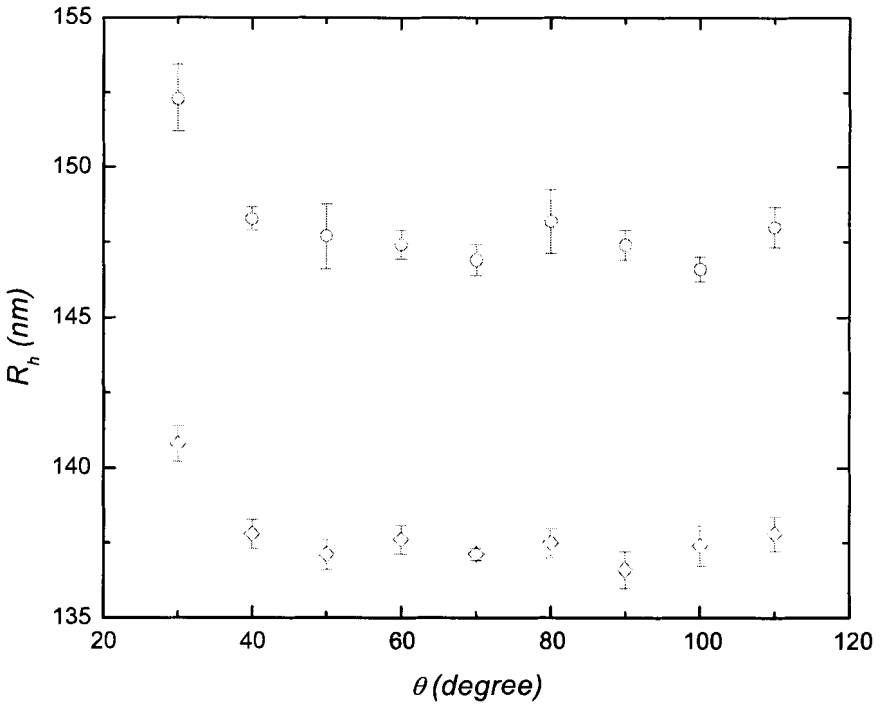

Figure B.7: Hydrodynamic radii as a function of scattering angle θ for $PNIPAM - 2$ at 36°C (○) and 40°C (◇).

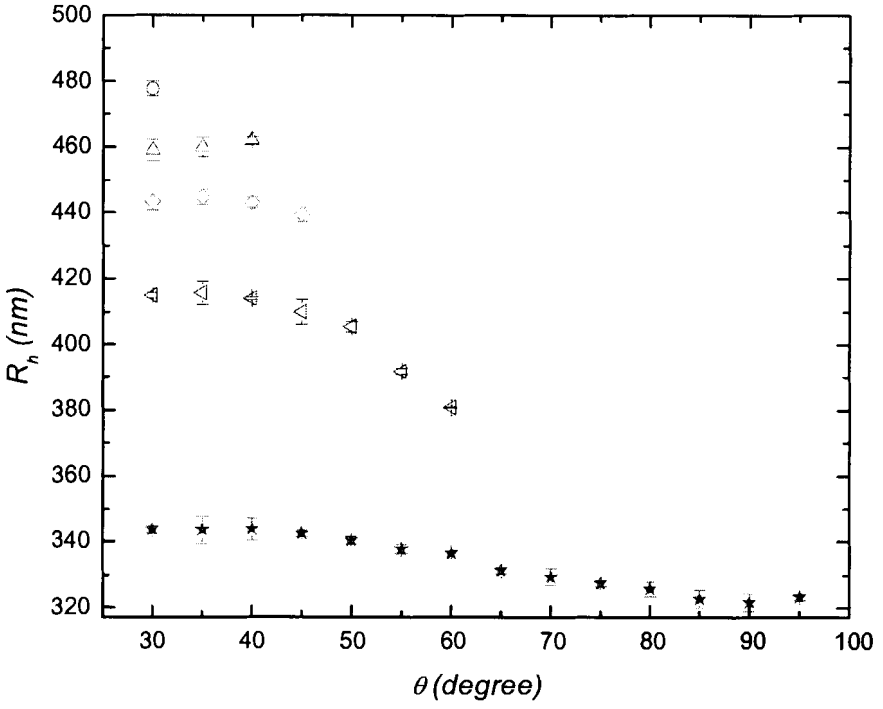

Figure B.8: Hydrodynamic radii as a function of scattering angle θ for $PNIPAM - 0$ at 25°C (○), 27°C (△), 29°C (◇), 31°C (◁) and 33°C (⋆).

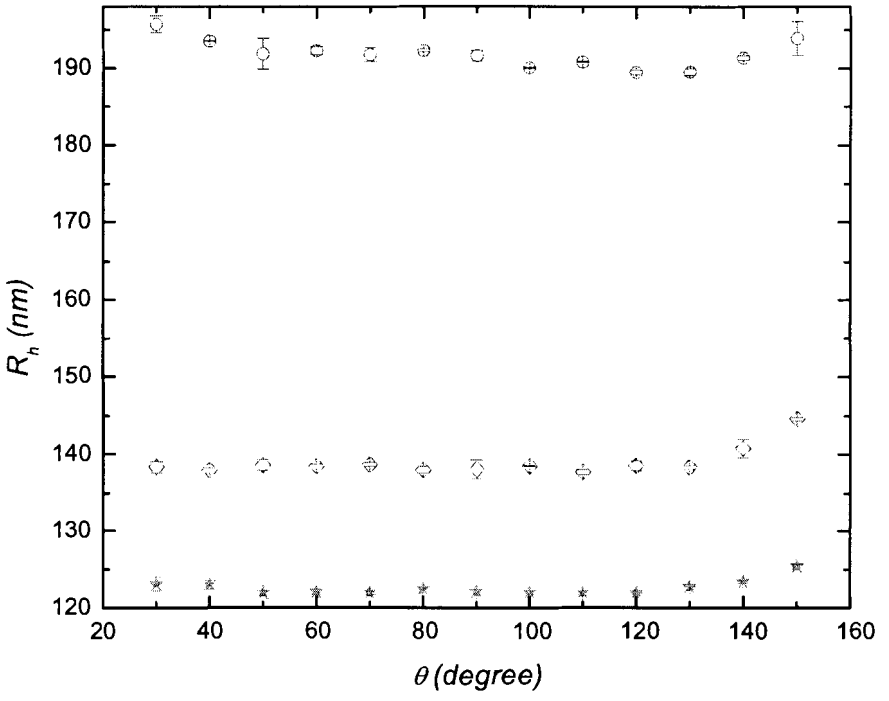

Figure B.9: Hydrodynamic radii as a function of scattering angle θ for $PNIPAM - 0$ at 34^oC ($\circ$), 36^oC ($\diamond$) and 40^oC ($\star$).

Bibliography

[1] B. H. Zimm. Apparatus and Methods for Measurement and Interpretation of the Angular Variation of Light Scattering; Preliminary Results on Polystyrene Solutions. J. Chem. Phys., 16:1099-1116, 1948.

[2] W. Burchard. Static and Dynamic Light Scattering from Branched Polymers and Biopolymers. Adv. Polym. Sci., 48:1-123, 1983.

[3] H. Schnablegger and O. Glatter. Simultaneous Determination of Size Distribution and Refractive Index of Colloidal Particles from Static Light-scattering Experiments. J. Colloid and Interface Sci.,158:228-242,1993.

[4] K. B. Strawbridge and F. R. Hallett. Size Distributions Obtained from the Inversion of I(Q) Using Integrated Light Scattering Spectroscopy. Macromolecules, 27:2283-2290, 1994.

[5] D. E. Koppel. Analysis of Macromolecular Polydispersity in Intensity Correlation Spectroscopy: The Method of Cumulants. J. Chem. Phys., 57:4814-4820, 1972.

[6] C. B. Bargeron. Measurement of a Continuous Distribution of Spherical Particles by Intensity Correlation Spectroscopy: Analysis by Cumulants. J. Chem. Phys., 61:2134-2138, 1974.

[7] J. C. Brown, P. N. Pusey and R. Dietz. Photon Correlation Study of Polydisperse Samples of Polystyrene in Cyclohexane. J. Chem.Phys., 62:1136-1144, 1975.

[8] B. J. Frisken. Revisting the Method of Cumulants for the Analysis of Dynamic Light-scattering Data. Appl. Opt., 40:4087-4091, 2001.

[9] F. R. Hallett, T. Craig, J. Marsh and B. Nickel. Particle Size Analysis: Number Distributions by Dynamic Light Scattering. Canadian Journal of Spectroscopy, 34:63-70, 1989.

[10] W. Brown. Dynamic Light Scattering: The Method and Some Applications. Clarendon Press, Oxford, 1993.

[11] G. Bryant, S. Martin, A. Budi and W. van Megen. Accurate Measurement of Small Polydispersities in Colloidal Suspensions. Langmuir, 19: 616-621, 2003.

[12] P. N. Pusey and W. van Megen. Detection of Small Polydispersities by Photon Correlation Spectroscopy. J. Chem. Phys., 80:3513-3520, 1984.

[13] S. U. Egelhaaf and P. Schurtenberger. Shape Transformations in the Lecithin-Bile Salt System: From Cylinders to Vesicles. J. Phys. Chem., 98:8560-8573, 1994.

[14] W. Burchard, K. Kajiwara and D. Nerger. Static and Dynamic Scattering Behavior of Regularly Branched Chains: A model of Soft-Sphere Microgels. J. Polym. Sci., 20:157-171, 1982.

[15] W. Burchard, M. Schmidt and W. H. Stockmayer. Information on Polydispersity and Branching from Combined Quasi-Elastic and Integrated Scattering. Macromolecules, 13:1265-1272, 1980.

[16] P. Pelton. Temperature-sensitive Aqueous Microgels. Adv. in Colloid and Interface Sci., 85:1-33, 2000.

[17] X. Zhang, D. Wu and C. Chu. Effect of the Crosslinking Level on the Properties of Temperature-Sensitive Poly(N-isopropylacrylamide) Hydrogels. J. Polym. Sci.: Part B: Polymer Physics, 41:582-593,2003.

[18] K. Kratz and W. Eimer. Swelling Properties of Colloidal Poly(N-isopropylacrylamide) Microgels in Solution. Ber. Bunsenges. Phys. Chem. 102: 848-854, 1998.

[19] J. Wu, B. Zhou and Z. Hu. Phase Behavior of Thermally Responsive Microgel Colloids. Phys. Rev. Lett., 90:(08304)1-4, 2003.

[20] C. Wu and S. Zhou. First Observation of the Molten Globule State of a Single Homopolymer Chain. Phys. Rev. Lett., 77:3053-3055, 1996.

[21] T. Hu and C. Wu. Clustering Induced Collapse of a Polymer Brush. Phys. Rev. Lett., 83:4105-4107, 1999.

[22] B. J. Berne and R. Pecora. Dynamic Light Scattering. Robert E. Krieger Publishing Company, Malabar, Florida, 1990.

[23] B. Chu. Laser Light Scattering: Basic Principles and Practice. Academic Press, Inc. New York, 1991.

[24] H. C. Van De Hulst. Light Scattering by Small Particles. Dover Publications, Inc. New York, 1981.

[25] K. S. Schmitz. An Introduction to Dynamic Light Scattering by Macromolecules. Academic Press, Inc. San Diego, 1990.

[26] A. F. Routh and W. Zimmerman. The Diffusion Coefficient of a Swollen Microgel Particle. J. Colloid and Interface Sci., 261:547-551, 2003.

[27] The ALV Manual of the version for ALV-5000/E for Windows, ALV-Gmbh, Germany, 1998.

[28] J. Gao and B. J. Frisken. Influence of Reaction Conditions on the Synthesis of Self-Cross-linked N-Isopropylacrylamide Microgels. Langmuir, 19:5217-5222, 2003.

[29] J. Gao and B. J. Frisken. Cross-Linker-Free N-Isopropylacrylamide Gel Nanospheres. Langmuir, 19:5212-5216, 2003.

[30] H. R. Haller, C. Destor and D. S. Cannell. Photometer for Quasielastic and Classical Light Scattering. Rev. Sci. Instrum. 54: 973-983, 1983

[31] P. R. Bevington and D. Keith Robinson. Data Reduction and Error Analysis for the Physical Sciences. McGraw-Hill Companies, Inc., 1992.

[32] D. R. Lide. CRC Handbook of Chemistry and Physics. CRC Press, Inc., 1994.

[33] K. Kratz, T. Hellweg and W. Eimer. Structural Changes in PNIPAM Microgel Particles as Seen by SANS, DLS and EM Techniques. Polymer, 42: 6631-6639, 2001.

[34] H. G. Schild. Poly(N-isopropylacrylamide) Experiment, Theory and Application. Prog. Polym. Sci. 17:163-249, 1992.

[35] P. J. Flory. Principles of Polymer Chemistry. George Banta Company, Inc. Wisconsin, 1967.

[36] K. Otake, H. Inomata, M. Konno and S. Satio. A New Model for the Thermally Induced Volume Phase Transition of Gels. J. Chem. Phys. 91:1345-1350, 1989.

[37] J. Pencer and F. R. Hallett. Effects of Vesicle Size and Shape on Static and Dynamic Light Scattering Measurements. Langmuir. 19, 7488-7497, 2003.

[38] J. H. van Zanten. The Zimm Plot and its Analogs as Indicators of Vesicle and Micelle Size Polydispersity. J. Chem. Phys. 102: 9121-9128, 1995.

[39] P. Molyneux. Water-Soluble Synthetic Polymers: Properties and Behavior. CRC Press, Inc., 1983.